THE UNIVERSITY OF

ARIZONA ®

TUCSON ARIZONA

December 20, 2001

VIA U.S. MAIL

Office of Naval Research
ATTN: Candace E. Wark
Ballston Centre Tower One
800 North Quincy Street
Arlington, VA 22217-5660
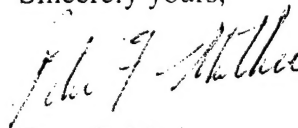
Subject: *Final Report Award No. N00014-99-1-0885*

Dear Dr. Wark:

Enclosed is Standard Form 298 for the above-referenced Final Report entitled *"Longitudinal Vortices in Turbulent Boundary Layers Subjected to Wall Curvature and Strong Adverse Pressure Gradients: Numerical Investigations Using LES and DNS"* submitted on behalf of Professor Hermann F. Fasel of our Department of Aerospace and Mechanical Engineering.

If you should have any questions or require additional information, please feel free to call either Professor Fasel at (520) 621-2771 or me at the number indicated on the letterhead.

Sincerely yours,

Peter F. Mather
Associate Director

PFM/poe

Enclosures

cc: Dr. Hermann F. Fasel

Office of Naval Research (SF 298 only)
Regional Office San Diego
4520 Executive Drive, Suite 300
San Diego, CA 92121-3019

Defense Technical Information Center (Final Technical Report w/SF 298)
8725 John J. Kingman Road, Suite 0944
Fort Belvoir, VA 22060-6218

Naval Research Laboratory (Final Technical Report w/SF298)
ATTN: CODE 5227
4555 Overlook Avenue SW
Washington, DC 20375-5320

REPORT DOCUMENTATION PAGE		Form Approved OMB No. 0704-0188

The public reporting burden for this collection of information is estimated to average 1 hour per response, including the time for reviewing instructions, searching existing data sources, gathering and maintaining the data needed, and completing and reviewing the collection of information. Send comments regarding this burden estimate or any other aspect of this collection of information, including suggestions for reducing the burden, to Department of Defense, Washington Headquarters Services, Directorate for Information Operations and Reports (0704-0188), 1215 Jefferson Davis Highway, Suite 1204, Arlington, VA 22202-4302. Respondents should be aware that notwithstanding any other provision of law, no person shall be subject to any penalty for failing to comply with a collection of information if it does not display a currently valid OMB control number.
PLEASE DO NOT RETURN YOUR FORM TO THE ABOVE ADDRESS.

1. REPORT DATE (DD-MM-YYYY) 20-Dec-2001	2. REPORT TYPE Final Report	3. DATES COVERED (From - To) 14Jun1999 to 13Jun 2001

4. TITLE AND SUBTITLE
Longitudinal Vortices in Turbulent Boundary Layers Subjected to Wall Curvature and Strong Adverse Pressure Gradients: Numerical Investigations Using LES and DNS

5a. CONTRACT NUMBER

5b. GRANT NUMBER
N00014-99-1-0885

5c. PROGRAM ELEMENT NUMBER

6. AUTHOR(S)
Hermann F. Fasel
Andreas Gross
Dieter Postl

5d. PROJECT NUMBER

5e. TASK NUMBER

5f. WORK UNIT NUMBER

7. PERFORMING ORGANIZATION NAME(S) AND ADDRESS(ES)
University of Arizona
Aerospace and Mechanical Engineering
Tucson, AZ 85721

8. PERFORMING ORGANIZATION REPORT NUMBER

9. SPONSORING/MONITORING AGENCY NAME(S) AND ADDRESS(ES)
Office of Naval Research Regional Office San Diego
4520 Executive Drive, Suite 300
San Diego, CA 92121-3019

20020103 026

12. DISTRIBUTION/AVAILABILITY STATEMENT
Approved for Public Release; distribution is Unlimited

13. SUPPLEMENTARY NOTES

14. ABSTRACT Longitudinal vortices in turbulent boundary layers that are subjected to strong wall curvature (both convex and concave) and strong adverse pressure gradients were investigated numerically. The motivation for this research was to uncover the fundamental mechanisms responsible for the generation of longitudinal vortices and their dynamical interaction with the other dominant coherent structures that arise from the presence of wall curvature and strong adverse pressure gradients. This understanding is essential for future implementation of separation control techniques for practical flows when longitudinal vortices are inherently present, or when forced longitudinal vortices are employed for separation control (i.e., on demand vortex generators). Furthermore, such investigations can shed light on the turbulence generation mechanisms for boundary layers subjected to streamwise curvature and pressure gradients when longitudinal vortices are present. The investigations were carried out using DNS, LES and unsteady RANS. Towards this end, we have employed our new Flow Simulation Methodology (FSM) for calculating turbulent flows. The present numerical investigations were a critical test for FSM and the turbulence model used in FSM as the investigated flows are highly complex with the turbulence in strong non-equilibrium.

15. SUBJECT TERMS

16. SECURITY CLASSIFICATION OF:			17. LIMITATION OF ABSTRACT	18. NUMBER OF PAGES	19a. NAME OF RESPONSIBLE PERSON Hermann F. Fasel
a. REPORT	b. ABSTRACT	c. THIS PAGE	SAR	63	19b. TELEPHONE NUMBER (Include area code) 520-621-2771
None	None	None			

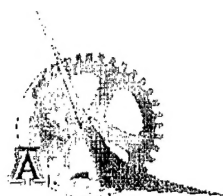Standard Form 298 (Rev. 8/98)
Prescribed by ANSI Std. Z39.18

Longitudinal Vortices in Turbulent Boundary Layers Subjected to Wall Curvature and Strong Adverse Pressure Gradients: Numerical Investigations Using LES and DNS

Final Report

by

Hermann F. Fasel, Andreas Gross, Dieter Postl

Department of Aerospace and Mechanical Engineering
University of Arizona
Tucson, AZ 85721

September 2001

Abstract

Longitudinal vortices in turbulent boundary layers that are subjected to strong wall curvature (both convex and concave) and strong adverse pressure gradients were investigated numerically. The motivation for this research was to uncover the fundamental mechanisms responsible for the generation of longitudinal vortices and their dynamical interaction with the other dominant coherent structures that arise from the presence of wall curvature and strong adverse pressure gradients. This understanding is essential for future implementation of separation control techniques for practical flows when longitudinal vortices are inherently present, or when forced longitudinal vortices are employed for separation control (i.e., on demand vortex generators). Furthermore, such investigations can shed light on the turbulence generation mechanisms for boundary layers subjected to streamwise curvature and pressure gradients when longitudinal vortices are present. The investigations were carried out using DNS, LES and unsteady RANS. Towards this end, we have employed our new Flow Simulation Methodology (FSM) for calculating turbulent flows. The present numerical investigations were a critical test for FSM and the turbulence model used in FSM as the investigated flows are highly complex with the turbulence in strong non-equilibrium.

Contents

1 Introduction

For practical hydrodynamic applications turbulent boundary layers arise that are subjected to various degrees of wall curvature, both concave and convex, and strong adverse/favorable pressure gradients. As a consequence, the resulting flows are highly complex, and the turbulence production mechanism, in particular, may be dominated by the presence of large coherent structures. In addition, these coherent structures may govern the separation behavior of the flow. Depending on the wall geometry, these structures may be predominantly two-dimensional, or strongly three-dimensional. The unique flow geometry of the so-called Stratford ramp yields a flow that is borderline between an attached and separated flow. A characteristic of the Stratford ramp geometry is that both curvature and strong adverse pressure gradients act on the boundary layer simultaneously. With the combined effect of strong pressure gradient and curvature, the flow along the Stratford ramp can be kept on the verge of separation (over the entire ramp region) without actually causing separation. With funding from a previous ONR grant, we have numerically investigated the turbulent boundary layer over a Stratford ramp [12, 16, 17]. Direct Numerical Simulations (DNS), Large-Eddy Simulations (LES) and Reynolds-averaged Navier-Stokes calculations of the laboratory experiments have been carried out in close collaboration with the experimental effort by Wygnanski and coworkers.

Although there was a large body of qualitative and quantitative agreement between simulations and experiments, there were systematic, unexplained differences between the simulations and experiments. In fact, from repeatedly scrutinizing the experimental and numerical evidence, it became clear to us that additional physical mechanisms must be present in the laboratory experiments that had not been captured by the simulations. For example, in all the numerical simulations, we could

1

never impose a pressure gradient strong enough to accomplish the rapid drop to almost zero skin friction immediately after the convex corner, as was possible in the experiments. In the simulations, the curvature at the convex corner had to be much less than in the experiments and, therefore, the pressure gradient at the initial region of the Stratford ramp was much less than in the experiments. As a consequence, the skin friction in this initial region was higher in the simulations than in the experiments. When a stronger curvature was imposed at the convex corners, such that it matched the experimental geometry, and the same adverse pressure gradient was imposed at the transition to the concave portion at the ramp, the boundary layer over the ramp would separate massively. Even with additional two-dimensional forcing, the flow could not be kept attached.

Further evidence of the systematic difference between experiments and simulations was obtained from simulations (LES, DNS) and RANS calculations of a flat plate boundary layer with the same adverse pressure gradient in the ramp region as in the experiment-thus the effects of curvature were eliminated. Again, in numerous attempts, we could never accomplish the low skin friction scenario over the ramp region as in the experiments. From these systematic differences of the results between simulations (with and without curvature) and the experimental measurements, we were in a position to draw two main conclusions: 1. The (concave) wall curvature in the Stratford ramp region is crucially important for obtaining the low skin friction values in the experiments, and thus for keeping the flow close to separation over the ramp region. 2. Longitudinal vortices may have been present in the experiments. Such vortices would effectively enhance an exchange of momentum and thus would allow for a more severe pressure drop in the initial Stratford ramp region without causing separation.

Indeed, when scrutinizing experimental data from another experiment (turbulent wall-jet over a Coanda cylinder), Wygnanski and coworkers found hard evidence that Görtler-type longitudinal vortices are present in this turbulent flow and that these vortices may significantly contribute to momentum transfer between the outer and inner regions, which helps to keep the flow attached (see Likhachev et al. [4]). Also, from these experiments, it was found that the observed size (the wave length λ_z) of the Görtler-type vortices scales directly with the (boundary) layer thickness ($|\lambda_z| \cong \delta$).

Upon obtaining the astonishing evidence that longitudinal, Görtler-type vortices do indeed play a crucial role in the separation behavior of turbulent Coanda wall jets, we re-evaluated our previous simulation data for the Stratford ramp flow and the experimental measurements of Wygnanski and coworkers to determine if the presence of Görtler-type vortices could possibly be responsible for the systematic discrepancy between simulations and experiments. From preliminary estimates and using averaged quantities (for example in the middle of the downstream extent of the concave ramp region), we found an approximate value for the Görtler number (the Görtler number is defined as $G = \mathrm{Re}_\vartheta \sqrt{\vartheta/R}$; Re_ϑ is the turbulent Reynolds number, $\mathrm{Re}_\vartheta = U_\infty \vartheta / \nu_T$; ϑ is the momentum thickness; ν_T is the turbulent viscosity) that was within the unstable region. This is an indication that Görtler type vortices can indeed arise in the Stratford ramp flow and may likely play an important role in our situation where the flow is close to separation and the exchange of momentum provided by such a large-scale (coherent) motion can decisively contribute toward prevention of separation.

Thus the question arises why Görtler vortices did not appear in our previous numerical simulations. The previous simulations were carried out with a spanwise domain size that was too small to accommodate the wave lengths of unstable Görtler vortices and, as a consequence, the generation of such vortices was suppressed. When planning the simulations, we deliberately used a small spanwise domain to allow for the highest possible resolution of the spanwise scales for a given number of grid points (to reduce the cost of the simulations). This was justified, as the consensus from previous experimental evidence of other investigations was that Görtler-type vortices did not play an important role in turbulent boundary layers [18, 19]; the exception being the paper by Tani [33]. The rationale for this conjecture was based on the assumption that turbulent diffusion would not allow the development of strong coherent longitudinal motion or that turbulent diffusion would destroy such coherent vortices when somehow already established (by upstream history or artificial vortex generators). However, as discussed above, it is possible that Görtler-type vortices may indeed be relevant. Also, we believe that their role in turbulent boundary layers may have been downplayed in the past because these vortices could not be reliably detected in the earlier experiments. Unequivocal identification of such vortices is associated with considerable experimental

difficulties (see Likhachev et al. [4]). In fact, in a more recent, preliminary DNS with a larger spanwise domain, we have found strong evidence that Görtler-type vortices are indeed present in this flow.

To investigate if Görtler vortices can indeed arise and play a role in a turbulent boundary layer on a concave wall, we initiated a new comprehensive numerical effort using Direct Numerical Simulations (DNS), Large Eddy Simulations (LES), as well as steady and unsteady RANS calculations. In particular, for these studies, we also wanted to employ our new Flow Simulation Methodology (FSM) that we have been developing (originally in collaboration with C. Speziale (Boston University)) during the past several years (for details see Speziale [15] and Zhang et al. [14]). In this report, the numerical investigations will be discussed that we carried out with funding from ONR for the past two years. (The investigations are not complete since the program was originally laid out for a three year duration.)

To obtain maximum pressure recovery for a given distance, wall bounded flows have to be kept close to separation. In 1959, Stratford showed how maximum flow deceleration and pressure recovery can be obtained in the shortest possible distance [9, 10]. For many technical applications, this type of flow may be desirable. Increased performance and efficiency of airfoils, diffusers, and many other devices could be obtained without the need for an increase in the spatial dimensions of the respective devices. As the flow is close to separation, minimal control effort can cause the flow to detach or attach.

Elsberry et al. extensively studied the Stratford ramp flow in wind tunnel measurements [2, 3]. They examined turbulence characteristics of the flow and studied the effect of external acoustic excitation. The extreme sensitivity of the flow to the upstream flow conditions is believed to be the reason for the difficulty of achieving a region of close to zero skin friction. As the flow approaches separation, a minimal increase of the pressure gradient along the contour can cause sudden, massive separation. In close collaboration with the experimental program, we have set up a program to investigate the Stratford ramp flow numerically.

The turbulent three-dimensional (3-D) Direct Numerical Simulations (DNS) by Zhang et al. [12,

13] were continued to get more statistical information. The turbulent DNS data was then decomposed into two-dimensional (2-D) and 3-D structures by means of a Proper Orthogonal Decomposition (POD). The 2-D structures were identified as spanwise vortices ("rollers") that propagate in streamwise direction. The 3-D structures were longitudinal vortices, probably caused by a Görtler type instability.

A temporal code was developed to better understand the phenomena of the Görtler instability mechanism. Using such a code with relatively little computational effort, a great number of Görtler-type simulations can be performed. A comparison of the longitudinal structures observed in the turbulent DNS with results of the temporal code shows qualitative agreement.

Furthermore, a compressible code for curvilinear coordinates was developed to study the 2-D and 3-D structures. First, the ramp geometry from wind tunnel experiments by Cullen et al. [23] was simulated. At first, by adjusting the molecular viscosity to turbulent levels, the effect of turbulence was crudely modeled. It could be shown that spanwise periodic forcing has a pronounced effect on the time averaged size of the separated region. For this geometry a steady 2-D RANS simulation yields a separation bubble in the concave section. The experiments by Wygnanski and our preliminary numerical simulations had indicated that the presence of large (spanwise) coherent structures contributes to an exchange of momentum between the inner and outer flow, thus helping to keep the flow attached. In a steady 3-D RANS computation, the impact of a forced longitudinal vortex on the separation bubble was investigated. Since this particular geometry resulted in a separation flow region, a more generic ramp geometry with smoother transitions between the various segments was constructed for the numerical simulations. As a result, attached flow was observed in 2-D RANS computations.

This generic ramp geometry (no separation in 2-D RANS) was used to study the influence of periodic spanwise forcing by blowing and suction on the separation characteristics of 2-D laminar flows. For this geometry we also employed our FSM for numerical simulations of turbulent flows both forced and unforced. The influence of the contribution function (used in FSM) on the flow structures was investigated. Using steady RANS calculations the dependence of the amplification of longitudinal vortices (initiated by steady spanwise disturbances) on the spanwise wavenumber

was studied. For wavenumbers smaller or larger than the optimal wavenumber, reduced growth of the longitudinal vortices was observed. In a separate computation, the longitudinal structures were forced by a corrugated wall. Finally, two unsteady fully three-dimensional FSM computations were initiated. Both unforced and steadily forced cases indicated the presence of longitudinal vortices in the temporal average. However, these results are preliminary as the simulations are not yet completed.

2 DNS of Turbulent Stratford Ramp Boundary Layer

For the 3-D turbulent DNS, the incompressible Navier-Stokes equations are solved in vorticity-velocity formulation [7, 8]. The incompressible code was originally developed by Meitz and Fasel [7, 8] for investigating transition in flat plate boundary layers. Superior amplitude and wave number accuracy is guaranteed by the underlying vorticity-velocity formulation of the governing equations, by a 4th-order accurate compact difference discretization in space and a 4th-order accurate Runge-Kutta time integration method as well as a spectral discretization in the spanwise direction. Later, the code was modified for the use of orthogonal curvilinear coordinates and for the FSM approach. The transformation of these equations to orthogonal curvilinear coordinates can be found in Zhang and Fasel [12, 13].

The inflow velocity $U_\infty = 15m/s$ was chosen in accordance with the experiments by Elsberry et al. [2, 3] and the computations by Zhang and Fasel [12, 13]. The Reynolds number based on the height of the ramp $h = 0.245m$ was $\text{Re}_h = 244,650$. A turbulent boundary layer profile taken from a turbulent boundary layer equation solver with $\text{Re}_\delta = 3,740$ was used as inflow condition. At the wall, the no-slip condition is imposed. Near the outflow boundary, a buffer domain technique is used to prevent reflections of disturbances. At the outflow boundary itself, all second derivatives in the streamwise direction are set to zero. At the freestream boundary, an adverse pressure gradient is imposed, which matches that of the experiments.

Typical results from a DNS are given in Fig. 2.1. Shown are isosurfaces and isocontours of instantaneous u. As the flow approaches the concave section, the boundary layer thickens considerably.
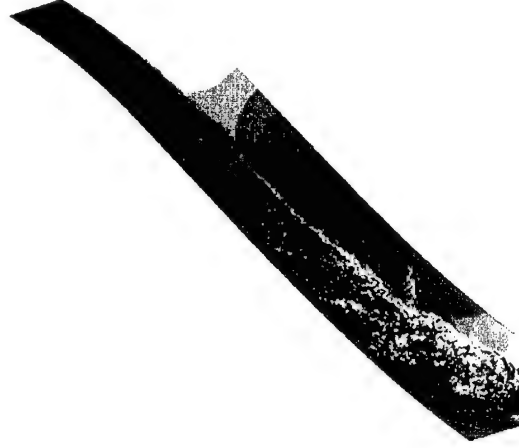
Figure 2.1: 3-D DNS. Isosurfaces of $u = 0.4, 0.5$ (blue, cyan),
and isocontours of u. Instantaneous picture.

A Proper Orthogonal Decomposition (POD) was performed for the purpose of investigating the results in more detail.

In POD, a given sequence of time- (time step n) and space- ($\vec{x}$) dependent flow data are decomposed into space-dependent eigenfunctions $\sigma_i(\vec{x})$ and time-dependent contribution functions $\zeta_i(t^n)$

$$\vec{u}(\vec{x}, t^n) = \sum_{i=1}^{i=I} \zeta_i(t^n)\vec{\sigma}_i(\vec{x}) \tag{2.1}$$

The resulting eigenfunctions are sorted by their respective "energy contents" (indicated by the magnitude of their corresponding eigenvalues). The mode 0 eigenfunction is generally the temporal average of the time-dependent flow data. This expansion of the flow field into "coherent structures" requires the smallest number of expansion terms for a given accuracy.

The first three modes of the POD are presented in Fig. 2.2, 2.3, and 2.4. The corresponding contribution functions are given in Fig. 2.5.

Mode 0 is the temporal average. Its eigenvalue has the value of 0.0227761865. The eigenfunction shows a spanwise modulation of all 3 velocity components in the concave section of the ramp (see Fig. 2.6). This is very likely due to the presence of longitudinal vortices in the flow believed to be
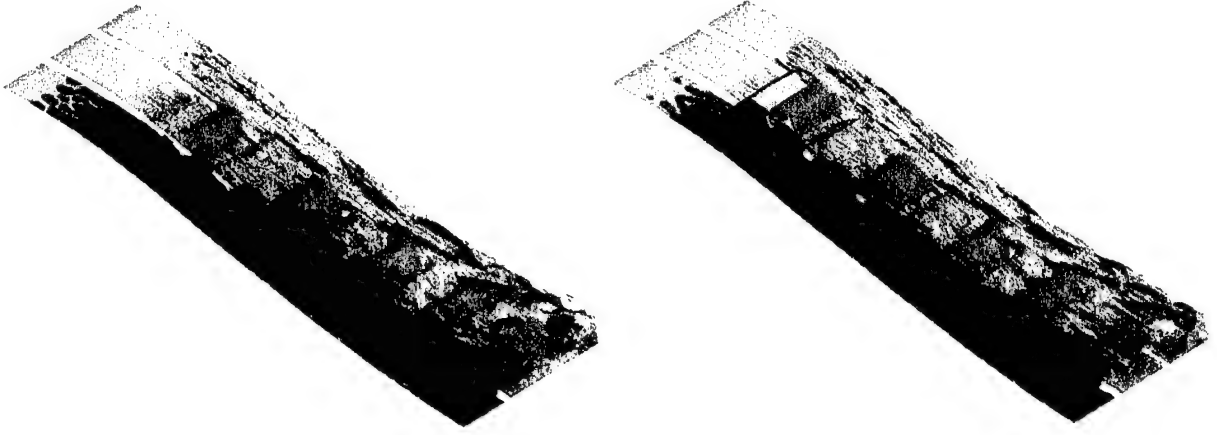
8

Figure 2.2: POD of 3-D DNS, mode 0. Isosurfaces of $u = 0.25, 0.5$ (red, blue), isosurfaces of $v = 0.007, 0.01$ (green, orange), and isosurfaces of $w = -0.01, 0.01$ (cyan, purple).
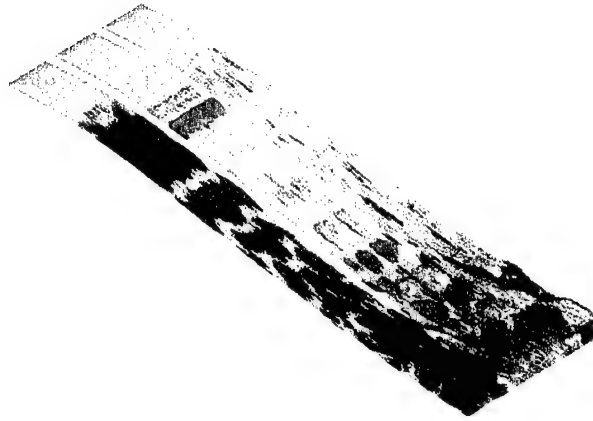

Figure 2.3: POD of 3-D DNS, mode 1. Isosurfaces of $u = -0.02, 0.02$ (red, blue), isosurfaces of $v = -0.01, 0.01$ (green, orange), and isosurfaces of $w = -0.01, 0.01$ (cyan, purple).

caused by a Görtler-type instability mechanism. A close-up of mode 0 in the concave section of the ramp is given in Fig. 2.7.

Figure 2.4: POD of 3-D DNS, mode 2 (left) and mode 3 (right). Isosurfaces of $u = -0.005, 0.005$ (red, blue), isosurfaces of $v = -0.003, 0.003$ (green, orange), and isosurfaces of $w = -0.005, 0.005$ (cyan, purple).
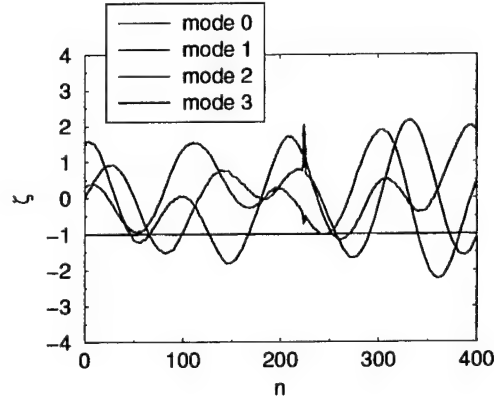
Figure 2.5: POD of 3-D DNS. Contribution function.

Mode 1, 2 and 3 oscillate with the same frequency. Mode 2 and 3 have about the same energy contents (eigenvalues 0.0000043412 and 0.0000039031). These modes appear to represent 2-D spanwise vortices (or "rollers") traveling downstream (see Fig. 2.8). Due to their motion, the POD resolves them with 2 modes that are essentially identical except for a phase shift by $1/4$ of their respective wavelengths.

Mode 1 is strongest in the concave section of the ramp. It is believed to represent the time-

Figure 2.6: POD of 3-D DNS, mode 0. Isosurfaces of $u = 0.5$ (cyan), $w = -0.01, 0.01$ (red, blue), isocontours of u (left), and isocontours of w (right).
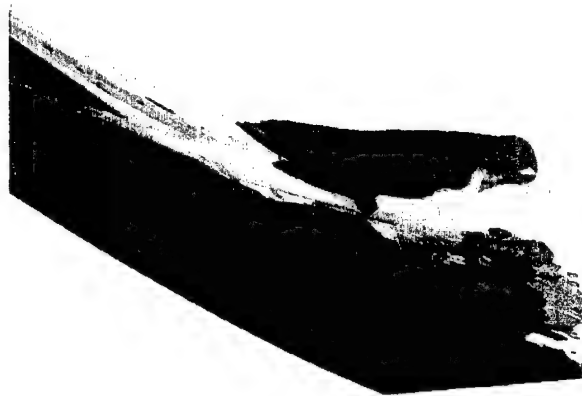
Figure 2.7: POD of 3-D DNS, mode 0. Close-up. Isosurfaces of $u = 0.5$ (cyan), $w = -0.01, 0.01$ (red, blue), and isocontours of u.

dependent interaction of the unsteady 2-D rollers with the steady 3-D longitudinal structures. Mode 1 contains more energy (eigenvalue 0.0000047336) than mode 2 and 3. The effect of this interaction on the separation behavior of the flow is not studied in this report. Instead, the two types of structures occuring in the flow field are investigated separately.

11
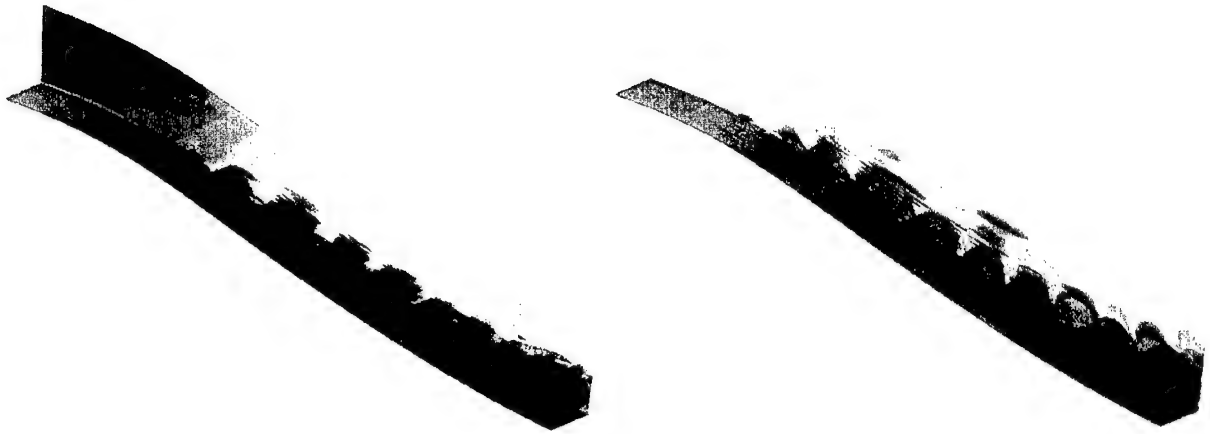
Figure 2.8: POD of 3-D DNS, mode 2. Isosurfaces of $u = -0.005, 0.005$ (red, blue) and isocontours of u (left). Isosurfaces of $v = -0.003, 0.003$ (red, blue), and isocontours of v (right).

3 Temporal Code

Most of our understanding of the role of Görtler vortices in turbulent boundary layer flows is based on results obtained from Direct Numerical Simulations of the full, nonlinear Navier-Stokes equations as discussed in chapter 2. While Direct Numerical Simulations most accurately represent the physics of the flows under consideration, they are very expensive to perform and do not lend themselves to investigations involving parameter studies, for example. In order to obtain further insight into phenomena associated with Görtler vortices in turbulent flows, additional tools are required. Towards this end, a temporal code was developed. Temporal numerical simulations differ from spatial numerical simulations in that, rather than providing a complete space-time history of the flow field, they allow for the flow to develop in time only and are assumed to be periodic in the downstream direction.

3.1 Governing equations

The temporal code is based on the incompressible, three-dimensional, unsteady Navier-Stokes equations in vorticity-velocity formulation. The coordinate system is a cylindrical one with azimuthal, radial and spanwise directions identified as θ, r and z.

Using the fact that both velocity and vorticity fields are solenoidal, the components of the transport equation for the vorticity can be written as

$$\frac{\partial \omega_\theta}{\partial t} = -\frac{\partial a}{\partial r} + \frac{\partial c}{\partial z} + \frac{1}{Re} \left\{ \frac{\partial}{\partial r} \left(\frac{1}{r} \frac{\partial}{\partial r} (r \omega_\theta) \right) + \frac{1}{r^2} \frac{\partial^2 \omega_\theta}{\partial \theta^2} + \frac{\partial^2 \omega_\theta}{\partial z^2} + \frac{2}{r^2} \frac{\partial \omega_r}{\partial \theta} \right\}, \quad (3.1)$$

13

$$\frac{\partial \omega_r}{\partial t} = \frac{1}{r}\frac{\partial a}{\partial \theta} - \frac{\partial b}{\partial z} + \frac{1}{Re}\left\{ \frac{\partial}{\partial r}\left(\frac{1}{r}\frac{\partial}{\partial r}(r\omega_r)\right) + \frac{1}{r^2}\frac{\partial^2 \omega_r}{\partial \theta^2} + \frac{\partial^2 \omega_r}{\partial z^2} - \frac{2}{r^2}\frac{\partial \omega_\theta}{\partial \theta}\right\}, \qquad (3.2)$$

$$\frac{\partial \omega_z}{\partial t} = -\frac{1}{r}\frac{\partial c}{\partial \theta} + \frac{\partial b}{\partial r} + \frac{b}{r} + \frac{1}{Re}\left\{ \frac{1}{r}\frac{\partial}{\partial r}\left(r\frac{\partial \omega_z}{\partial r}\right) + \frac{1}{r^2}\frac{\partial^2 \omega_z}{\partial \theta^2} + \frac{\partial^2 \omega_z}{\partial z^2}\right\} \qquad (3.3)$$

where a, b and c are the non-linear terms

$$a = v_r\omega_\theta - v_\theta\omega_r, \qquad (3.4)$$

$$b = v_z\omega_r - v_r\omega_z, \qquad (3.5)$$

$$c = v_\theta\omega_z - v_z\omega_\theta. \qquad (3.6)$$

In addition to the transport equations, three Poisson-type equations have to be solved for the velocity components v_θ, v_r and v_z:

$$\frac{\partial^2 v_\theta}{\partial r^2} + \frac{1}{r}\frac{\partial v_\theta}{\partial r} - \frac{v_\theta}{r^2} + \frac{1}{r^2}\frac{\partial^2 v_\theta}{\partial \theta^2} + \frac{\partial^2 v_\theta}{\partial z^2} + \frac{2}{r^2}\frac{\partial v_r}{\partial \theta} = \frac{\partial \omega_z}{\partial r} - \frac{\partial \omega_r}{\partial z}, \qquad (3.7)$$

$$\frac{\partial^2 v_r}{\partial r^2} + \frac{1}{r}\frac{\partial v_r}{\partial r} - \frac{v_r}{r^2} + \frac{1}{r^2}\frac{\partial^2 v_r}{\partial \theta^2} + \frac{\partial^2 v_r}{\partial z^2} - \frac{2}{r^2}\frac{\partial v_\theta}{\partial \theta} = \frac{\partial \omega_\theta}{\partial z} - \frac{1}{r}\frac{\partial \omega_z}{\partial \theta}, \qquad (3.8)$$

$$\frac{\partial^2 v_z}{\partial r^2} + \frac{1}{r}\frac{\partial v_z}{\partial r} + \frac{1}{r^2}\frac{\partial^2 v_z}{\partial \theta^2} + \frac{\partial^2 v_z}{\partial z^2} = \frac{1}{r}\frac{\partial \omega_r}{\partial \theta} - \frac{1}{r}\frac{\partial}{\partial \theta}(r\omega_\theta). \qquad (3.9)$$

In accordance with the underlying assumptions of the temporal model, the flow is assumed to be periodic in the streamwise (azimuthal) direction. Periodicity is also assumed in the spanwise direction, which allows for the flow variables to be expanded in Fourier series in both θ- and z-directions.

The temporal code was originally adapted from the spatial code developed by Meitz and Fasel [7, 8]. The numerical treatment of the governing equations is therefore very similar.

3.2   Görtler instability

Rayleigh showed in 1916 [24] that

$$\frac{d(\Gamma^2)}{dr} < 0, \text{ anywhere in the flow} \qquad (3.10)$$

14
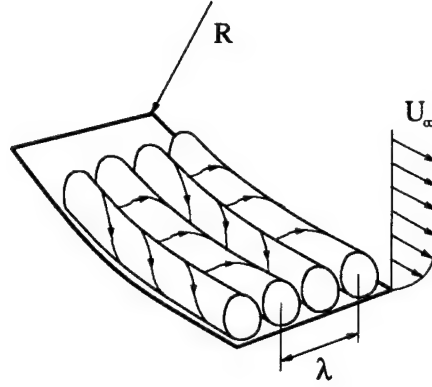
Figure 3.1: Schematic view of Görtler vortices within a boundary
layer over a concave wall.

is a sufficient condition for the existence of an inviscid axisymmetric instability. Γ is the circulation
defined as $\Gamma = rv$. This Rayleigh circulation criterion states that boundary layers on concave walls
and wall jets on convex walls can become unstable [25]. In 1941, Görtler showed the solution of
the disturbance equations to be in the form of streamwise-oriented, counter-rotating vortices [26].

Fig. 3.1 schematically illustrates Görtler vortices in a laminar boundary layer along a concave
surface. R is the local wall radius of curvature, λ is the spanwise wavelength of the disturbances
and U_∞ is the boundary layer freestream velocity. The disturbance velocities associated with the
spanwise vortices grow in streamwise direction while maintaining their spanwise wavelength.

The Görtler number is defined as

$$G = \frac{U_\infty \vartheta}{\nu} \sqrt{\frac{\vartheta}{R}} = \mathrm{Re}_\vartheta \sqrt{\frac{\vartheta}{R}}, \tag{3.11}$$

where ϑ is the local momentum thickness and ν is the kinematic viscosity, and the spanwise
wavenumber

$$k = \frac{2\pi\vartheta}{\lambda}. \tag{3.12}$$

Various different neutral curves for the onset of the Görtler instability have been proposed in the
past. In this report, the neutral curve of Hall (1983) [27] was chosen for the validation of the
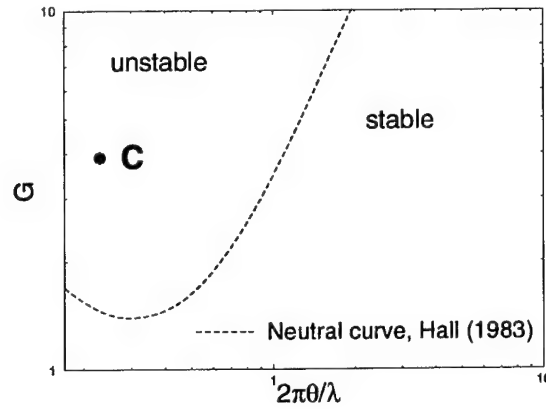temporal code.

3.3 Validation
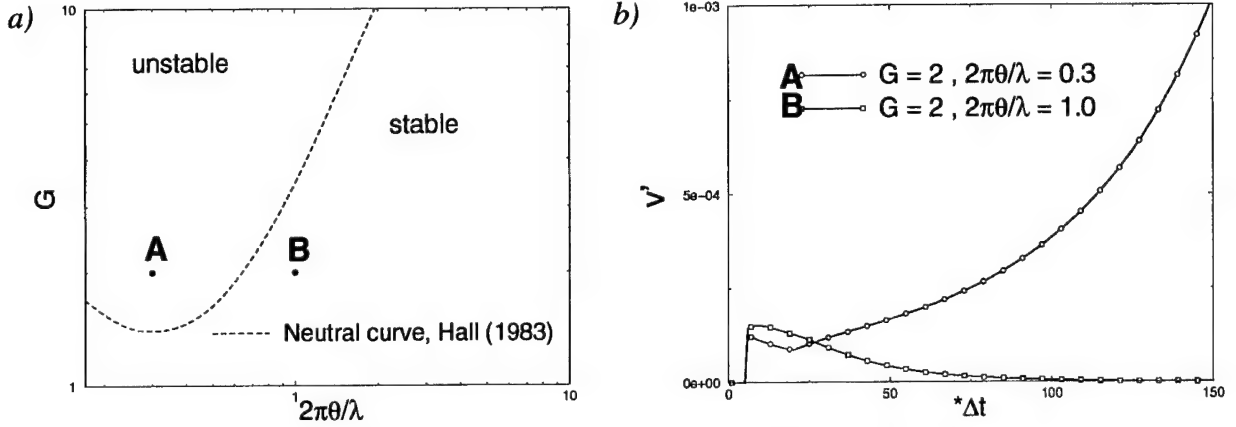
Figure 3.2: Temporal code. Test cases A and B. *a)* Görtler stability diagram. *b)* Time-development of wall-normal disturbance.

Before applying the temporal code for DNS of turbulent Görtler flows extensive test calculations were performed for laminar Görtler flows in order to validate the newly developed code. Results of typical test cases of such validation calculations are discussed below.

Two different combinations of G and k are chosen. For case A, G is set to 2 and k is set to 0.3. This combination is in the unstable region of Hall's neutral curve. Case B, defined by $G = 2$ and $k = 1$, lies in the stable region (see Fig. 3.2).

The temporal development of the maximum wall-normal disturbance velocity component is shown in Fig. 3.2. It is obvious that the calculations predict exponential growth for case A and exponential decay for case B. This is in agreement with linear stability theory (the initial disturbance was very small).

For the purpose of studying the time-evolution of a Görtler unstable flow, a test case C well within the unstable region with $G = 3.9$ and $k = 0.23$ (see Fig. 3.3) was computed. Instantaneous results are plotted in Fig. 3.4. The contours of constant streamwise velocity u (Fig. 3.4*a*) are a good indicator for the shape of the boundary layer while the spanwise velocity w (Fig. 3.4*b*) is a good indicator for the location and strength of the Görtler vortices. Since $w_\infty = 0$, the spanwise velocity w is equal to the spanwise component w' of the disturbance velocity.

16

Figure 3.3: Temporal code. Görtler stability diagram for test case C.
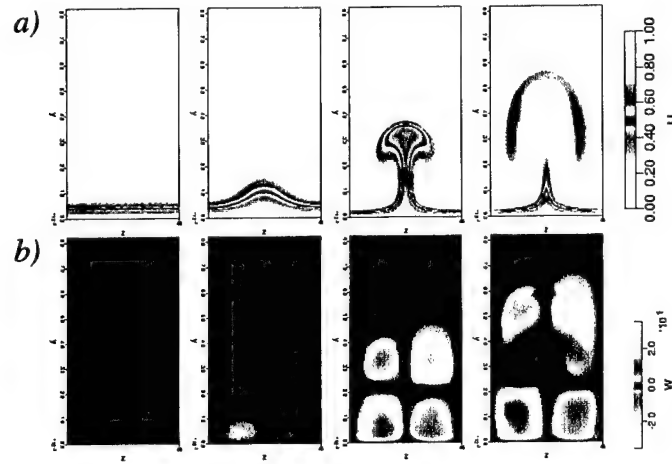
Figure 3.4: Temporal code. Color-contours of *a)* streamwise velocity u and *b)* spanwise velocity w (bottom).

The strong growth of the Görtler vortices distorts the boundary layer profile. Note that one pair of vortices is simulated (periodic boundary conditions in spanwise direction). As the Görtler vortices reach nonlinear stages, the boundary layer becomes highly distorted. The mushroom-like deformation of the streamwise velocity leads to local high-shear layers in the outer region of the boundary layer. Similar observations can be found in Saric [25] and in Swearingen and Blackwelder [29].

3.4   Qualitative comparison of temporal laminar DNS and spatial turbulent DNS

Sabry and Liu (1991) [28] have shown that boundary layer flows over concave surfaces lend themselves to qualitative comparison with computations obtained using the temporal model. They obtained good agreement with experiments by Swearingen and Blackwelder [29] well into the nonlinear regime.
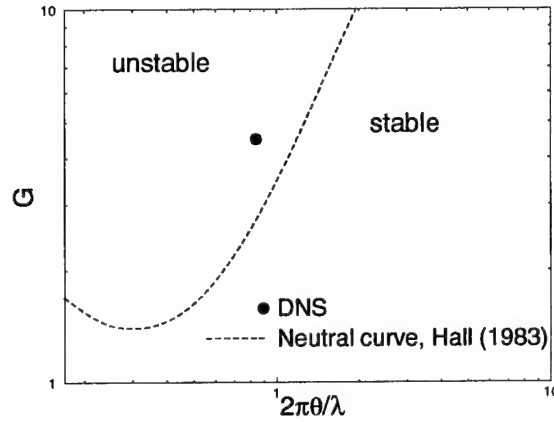
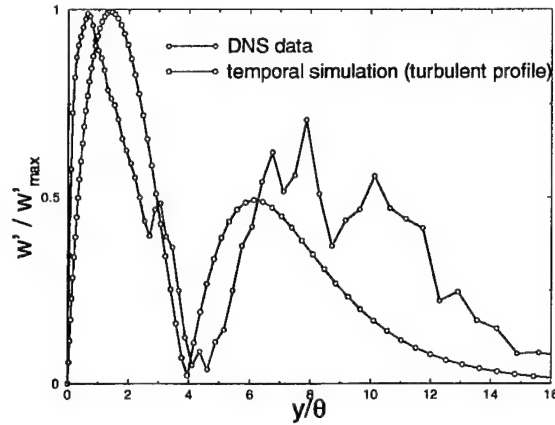**Figure 3.5:** Görtler stability diagram for turbulent DNS.
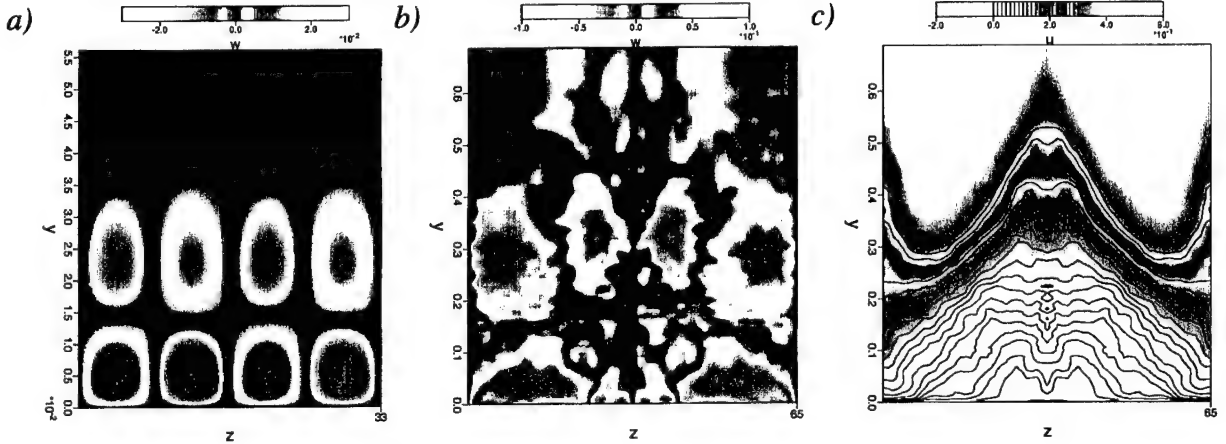
Figure 3.6: Color-contours. *a)* Spanwise velocity w obtained from temporal simulation. *b)*, *c)* Spanwise velocity w and streamwise velocity u (cross-sectional view at ramp exit) obtained from DNS of full geometry.

A temporal DNS with $G = 4.5$ and $k = 0.84$ (case D) was performed for qualitative comparison

Figure 3.7: Comparison of DNS data with temporal simulation
(case D). Eigenfunctions.

with results from the turbulent DNS.

Fig. 3.5 indicates that the time-averaged velocity profile obtained from the turbulent DNS in the concave section of the ramp is Görtler unstable (using $\nu_t = 100\nu_{sp}$; ν_{sp} is the laminar viscosity of the spatial DNS; the spanwise wave number was specified by the spanwise size of the integration domain). This is consistent with the appearance of longitudinal structures in the DNS results. The temporal simulation was performed using the time-averaged velocity profile as the baseflow (and $\nu = 100\nu_{sp}$). A cross-sectional view of the turbulent DNS results as well as an instantaneous plot of the temporal simulation are given in Fig. 3.6. Plotted are contours of the spanwise velocity component from the temporal simulation (left) as well as from the DNS (center). In addition, the deformation of the streamwise velocity contours of the DNS is shown (right).

The temporal simulation shows two staggered pairs of vortices in the spanwise direction (see Fig. 3.6a). The turbulent DNS also shows four vortices (see Fig. 3.6b). Despite of the high level of turbulent fluctuations and the limited amount of data available for the time-average, the structures are clearly visible. The distorted boundary layer of the turbulent DNS (see Fig. 3.6c) simulation also compares well with temporal results (see Fig. 3.4). The conclusion drawn in chapter 2, that the longitudinal structures may be associated with Görtler vortices, is substantiated.

The amplitude distributions from the temporal simulation and the turbulent DNS are compared in Fig. 3.7. The distinct shape of the spanwise velocity distribution of Görtler vortices can clearly

be identified in the result obtained from the DNS. It is believed that additional data would further improve the agreement.

The existence of longitudinal vortices as coherent structures in turbulent boundary layers remains a highly debated topic. Some authors reject the idea altogether (see Patel and Sotiropoulos [30], Barlow and Johnston [31]), others claim the opposite (see Tani [33], Moser and Moin [32]). The latter propose that the apparent eddy viscosity governs the flow in the same way the molecular viscosity does in the laminar case. Assuming a constant eddy viscosity of $\nu_T = 0.018 U_\infty \delta^*$ (δ^* is the displacement thickness) and $\delta^* = 1.3\vartheta$ Tani arrives at the following approximate expression for the Görtler number in turbulent flows

$$G = 43\sqrt{\frac{\vartheta}{R}} \, .$$
(3.13)

The idea of coherent Taylor vortices existing in turbulent closed-system flows is generally undisputed. The question remains to be answered whether Görtler vortices in open flow systems along concave surfaces represent the direct analogy to Taylor-type flows.

All the evidence presented in this work supports the existence of Görtler vortices in the turbulent Stratford ramp boundary layer.

4 Compressible code in curvilinear coordinates

In addition to the incompressible code discussed in the previous chapter, we developed a code based on the compressible Navier-Stokes equations. This was done for the purpose of creating a Navier-Stokes code for more general applications. Navier-Stokes codes based on the compressible Navier-Stokes equations are generally easier to parallelize than incompressible codes and are thus more suitable for today's massively parallel computers. Since compressibility effects are insignificant in Stratford ramp applications associated with this particular research, calculations were carried out at a Mach-number of 0.25.

The new code is based on the compressible Navier-Stokes equations in conservative form

$$\frac{\partial \vec{Q}}{\partial t} + \frac{\partial \vec{\mathcal{E}}}{\partial x} + \frac{\partial \vec{\mathcal{F}}}{\partial y} + \frac{\partial \vec{\mathcal{G}}}{\partial y} = \frac{\partial \vec{\mathcal{E}}_v}{\partial x} + \frac{\partial \vec{\mathcal{F}}_v}{\partial y} + \frac{\partial \vec{\mathcal{G}}_v}{\partial y}, \tag{4.1}$$

where $\vec{Q} = [\rho, \rho u, \rho v, \rho w, \rho e]^T$ is the state vector,

$$\vec{\mathcal{E}} = \left[\rho u, \rho u^2 + p, \rho uv, \rho uw, (\rho e + p)u\right]^T \tag{4.2}$$

$$\vec{\mathcal{F}} = \left[\rho v, \rho vu, \rho v^2 + p, \rho vw, (\rho e + p)v\right]^T \tag{4.3}$$

$$\vec{\mathcal{G}} = \left[\rho w, \rho wu, \rho wv, \rho w^2 + p, (\rho e + p)w\right]^T \tag{4.4}$$

are the convective flux vectors, and

$$\vec{\mathcal{E}}_v = \left[0, \tau_{xx}, \tau_{xy}, \tau_{xz}, \tau_{xx}u + \tau_{xy}v + \tau_{xz}w + \kappa\frac{\partial T}{\partial x}\right]^T \tag{4.5}$$

$$\vec{\mathcal{F}}_v = \left[0, \tau_{xy}, \tau_{yy}, \tau_{yz}, \tau_{xy}u + \tau_{yy}v + \tau_{yz}w + \kappa\frac{\partial T}{\partial y}\right]^T \tag{4.6}$$

21

$$\vec{\mathcal{G}}_v = \left[0, \tau_{xz}, \tau_{yz}, \tau_{zz}, \tau_{xz}u + \tau_{yz}v + \tau_{zz}w + \kappa\frac{\partial T}{\partial z}\right]^T \tag{4.7}$$

are the viscous flux vectors. The heat conductivity κ is computed from the dynamic viscosity μ by means of the Prandtl analogy with constant Prandtl number Pr $= 0.72$ and isentropic exponent $\gamma = 1.4$. The Sutherland law is used to compute μ. The equation of state $p = \rho RT$ closes the formulation. Since most surfaces of technical interest are complex the equations are transformed into generalized curvilinear coordinates (for details see Visbal and Gordnier [11]).

For Reynolds Averaged Navier-Stokes (RANS) computations, two additional transport equations,

$$\frac{\partial \rho k}{\partial t} + \nabla \cdot (\rho \vec{v} k) = \nabla \cdot ((\mu + \sigma^* \mu_T)\nabla k) \tag{4.8}$$

$$+ \quad P_k - \beta^* \rho k \omega \tag{4.9}$$

$$\frac{\partial \rho \omega}{\partial t} + \nabla \cdot (\rho \vec{v} \omega) = \nabla \cdot ((\mu + \sigma^* \mu_T)\nabla \omega) \tag{4.10}$$

$$+ \quad \alpha \frac{\rho}{\mu_T} P_k - \beta \rho \omega^2 \tag{4.11}$$

for the turbulence kinetic energy k and dissipation rate ω need to be solved. The model constants and the definition of the production $\mathcal{P}$ and destruction terms $\mathcal{D}$ can be found in Wilcox [5] ($\alpha = 5/9$, $\beta = 3/40$, $\beta^* = 9/100$, $\sigma^* = 1/2$). The turbulence equations are coupled with the mean flow equations via the eddy viscosity $\mu_T = \rho k/\omega$, which is added to the molecular viscosity μ.

For the Flow Simulation Methodology (FSM) which we have been developing originally with C. Speziale, (see [15]) we are using a modified contribution function (see Zhang et al. [14])

$$f = 1 - \exp\left(-\frac{\max(0, \frac{\Delta}{L_k} - 2)}{N}\right) \tag{4.12}$$

where

$$\Delta = \sqrt{(\Delta x)^2 + (\Delta y)^2 + (\Delta z)^2} \tag{4.13}$$

is an averaged local grid spacing. L_k is the Kolmogorov length scale

$$L_k = \left(\frac{\nu^3}{c_\mu \omega k}\right)^{\frac{1}{4}} \tag{4.14}$$

with $c_\mu = 0.09$. The parameter N is specified by the user. The feedback of the turbulence quantities into the N-S equations is scaled by f, e.g. the Reynolds stresses or the eddy viscosity are multiplied by f.

4.1   Numerical scheme and grid generation

The convective terms in equation 4.1 are discretized by a 5th- (for the RANS computations) and 9th-order upwind scheme (for the laminar computations) based on a WENO extrapolation [20, 21] and the Roe scheme [22]. The discretization of the viscous terms is 4th order accurate. For the turbulence equations, a stable second order accurate discretization was chosen.

For explicit computations, a four-stage 4th-order accurate Runge-Kutta time integration scheme (see Harris [34]) is used. For implicit time stepping, a second-order accurate Adams-Moulton method (see Ferziger [35]) is used. For the latter the resulting system of equations is solved by a line Gauss-Seidel method.

For the grid generation, a Poisson solver developed by Israel and Fasel [6] is used to minimize the grid deviation from orthogonality everywhere in the domain.

4.2   Boundary conditions

For "incompressible" Stratford Ramp calculations, the inflow Mach-number is set to 0.25. For RANS computations, the original Reynolds number Re_h is used. For 2-D laminar computations, a constant eddy viscosity of $\mu_T/\mu = 100$ is assumed. This value is believed to be a reasonable spatial average of the eddy viscosity encountered within a typical turbulent boundary layer. The Reynolds number Re_h is lowered accordingly. The ratio of momentum thickness Reynolds number Re_ϑ to Re_h at the inflow boundary is held constant. The compressible laminar boundary layer equations [1] are solved numerically to obtain the self-similar compressible boundary layer profile which serves as inflow boundary condition. At the inflow boundary, the static pressure is extrapolated from the computational domain to allow upstream traveling acoustic waves to leave the computational domain. At the outflow boundary, temperature and velocities are extrapolated, the static pressure is fixed. In a confined region close to the outflow, volume forcing is employed to prevent flow structures from accumulating near the outflow boundary and contaminating the flow

field upstream of the outflow boundary. For 3-D simulations, symmetry is enforced at the spanwise boundaries.

Body-fitted calculations enable us to simulate the entire relevant wind tunnel test section of the experiments by Elsberry et al. [2, 3].To avoid excessive use of computational resources, the upper wall is treated as a no-stress wall. The lower curved wall is set to be adiabatic.

4.3 Validation

4.3.1 Laminar test case
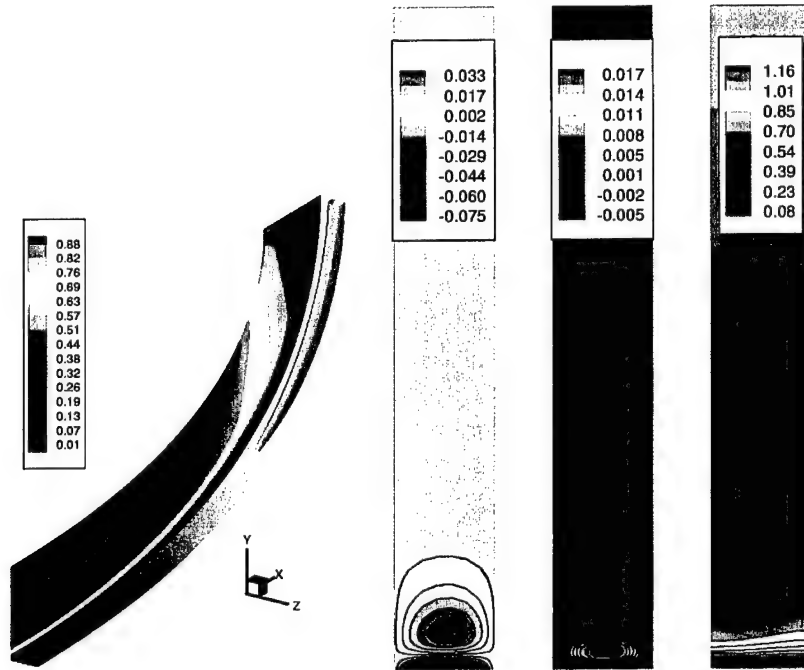
Figure 4.1: Isosurface $\omega_y = 0.005$ and u isocontours (left), ω_y isocontours, w isocontours, and v isocontours (right).

A simple laminar test case was chosen to study the evolution of longitudinal structures on a curved wall. The contour was designed to have a smooth increase in curvature in streamwise direction such that separation is avoided. The inflow Reynolds number was $\mathrm{Re}_x = 3.3 \cdot 10^3$. The initial radius was $\mathrm{Re}_{R1} = 4.12 \cdot 10^4$ and the end radius was $\mathrm{Re}_{R2} = 4.12 \cdot 10^3$. The flow makes a 90°

24

degree turn. A longitudinal vortex was forced by application of steady blowing and suction close to the inflow. The longitudinal vortex becomes stronger as the curvature increases (see Fig. 4.1). As in the temporal simulation, the boundary layer profile is distorted by the Görtler vortex (see u isocontours). The w isocontours show the typical behavior.

4.3.2   Turbulent test case
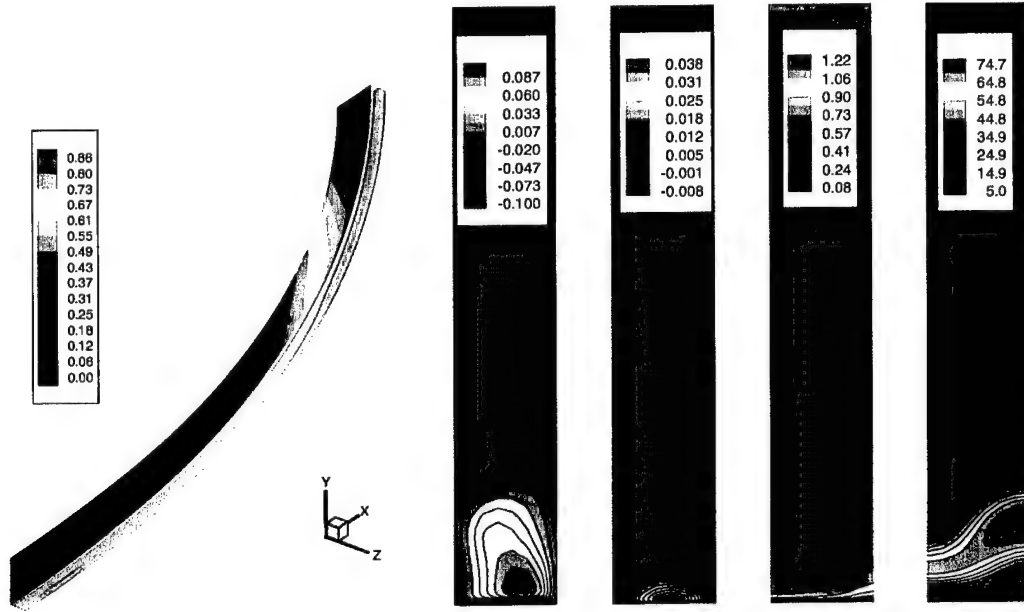
Figure 4.2: Isosurface $\omega_y = 0.03$ and u isocontours (left), ω_y iso-
contours, w isocontours, v isocontours, and μ_T/μ iso-
contours (right).

For the same geometry as before, a calculation was performed with the turbulence model turned on. The inflow Reynolds number was set to $\mathrm{Re}_x = 3.3 \cdot 10^5$. The start radius now was $\mathrm{Re}_{R1} = 4.12 \cdot 10^6$ and the end radius was $\mathrm{Re}_{R2} = 4.12 \cdot 10^5$. The flow looks qualitatively similar to the laminar test case. The steady longitudinal vortex is strongly amplified in the section of high curvature, the boundary layer profile is distorted due to the presence of the steady vortices. This clearly indicates that Görtler vortices can also emerge in steady RANS calculations.

5 Stratford Ramp Geometry 1

First, we simulated the flow for the ramp geometry (ramp 1) used in the experiments by Cullen et al. [23]. This ramp geometry, while causing the flow to stay attached in the experiments, resulted in flow separation in our steady RANS computations. This may be due either to the turbulence model used, to an inconsistency in the state of the inflow boundary layer or to the fact that steady RANS cannot represent effects of unsteady large structures. Since separation was undesirable for the current investigations, a more benign generic ramp geometry was designed and studied (ramp 2, see chapter 6). For the computations presented in this chapter (using ramp 1), a slip wall is assumed at the upper boundary.

Two dominant structures, 2-D spanwise rollers and 3-D longitudinal vortices, were found to govern the Stratford ramp flow. A prudent way to gain more understanding of these two underlying mechanisms is to study them independently from each other. The unsteady spanwise vortices are investigated in 2-D laminar, 2-D RANS and 2-D "FSM" computations. The steady 3-D structures are studied in 3-D RANS and 3-D FSM computations.

5.1   2-D "laminar" computations

To approximately "model" the effect of turbulence

$$\frac{\mu_T}{\mu} = 100 \tag{5.1}$$

was used for the 2-D "laminar" computations.

5.1.1   Unforced case
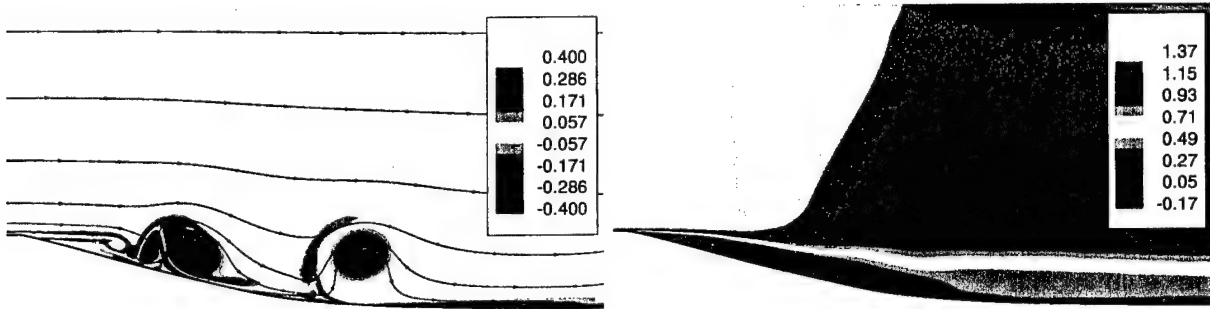
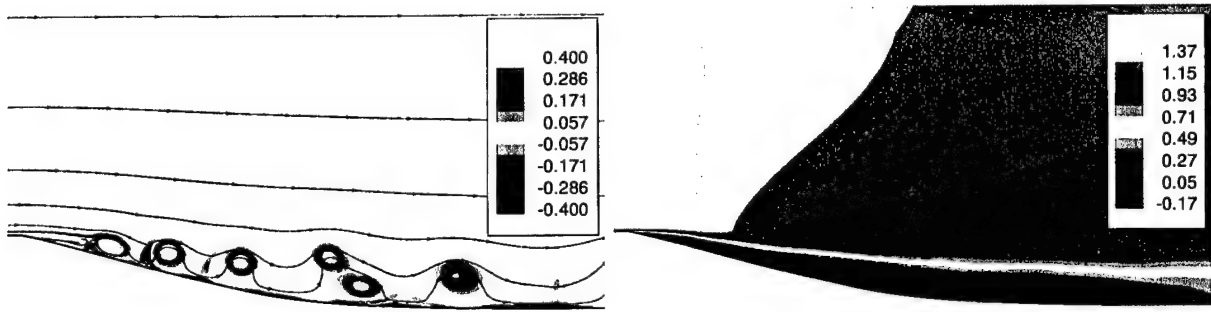**Figure 5.1:** 2-D "laminar" computation. ω_z isocontours (instantaneous) (left) and u isocontours (time averaged) (right).
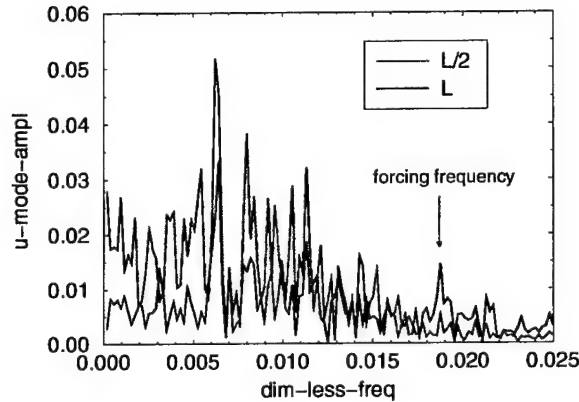
Figure 5.2: 2-D "laminar" computation. Frequency spectrum of u velocity oscillations of unforced calculation at different downstream locations (L is the ramp length).

Initially, calculations were performed without introducing any "controlled" disturbances. The results form these computations show large spanwise "rollers" and a significant separation bubble (see Fig. 5.1) at the beginning of the concave part of the ramp. The u-velocity signal taken at 2 downstream locations (see Fig. 5.2) exhibits a fairly broad spectrum. Small, high frequency vortices merge early on to form large, slowly rotating, low frequency vortices that cause the boundary layer to thicken considerably in the mean.

Figure 5.3: 2-D "laminar" computation. ω_z isocontours (instantaneous) (left) and u isocontours (time averaged) (right).

5.1.2   Forced case

By means of a blowing and suction slot upstream of the ramp, time periodic disturbances were introduced into the flow. The appearance of the spanwise "rollers" was significantly altered compared to the unforced case (see Fig. 5.3). Different forcing frequencies were investigated. The higher frequency range was most efficient in reducing the size of the separation bubble. This exchange of momentum is the cause for the reduction in size of the separation bubble. The time averaged boundary layer for the forced case is considerably thinner than for the unforced case.

Since the turbulent DNS shows similar spanwise rollers (see Fig. 2.8) it is very likely that the separation behavior of the turbulent Stratford ramp flow can also be modified by periodic spanwise blowing and suction.

5.2   2-D steady RANS

The results of a steady 2-D RANS simulation are presented in Fig. 5.4. In contrast to the experiments, a separation bubble can be observed in the concave section of the ramp. Due to the strong adverse pressure gradient, the boundary layer thickness is greatly increased. The maximum ratio of eddy viscosity to molecular viscosity is about 1500. A glance at the skin friction coefficient (see Fig. 5.8) reveals the exact size of the separation bubble.
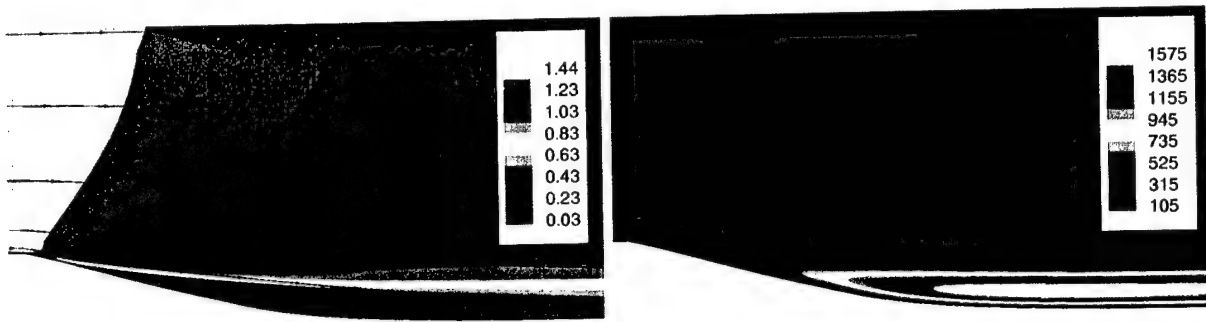
Figure 5.4: 2-D steady RANS. u isocontours (left) and μ_T/μ iso-contours (right).

5.3 2-D "FSM" computations

The experiments have revealed the presence of large scale coherent structures in the flow. The dynamics of these structures cannot be captured by steady RANS. Therefore, 2-D "FSM" calculations were carried out The factor N in the contribution function f (see eq. 4.12) was chosen to be 13000. Due to the inherent three-dimensionality of turbulence, the 2-D "FSM" can only capture the effect of 2-D large-scale coherent structures.
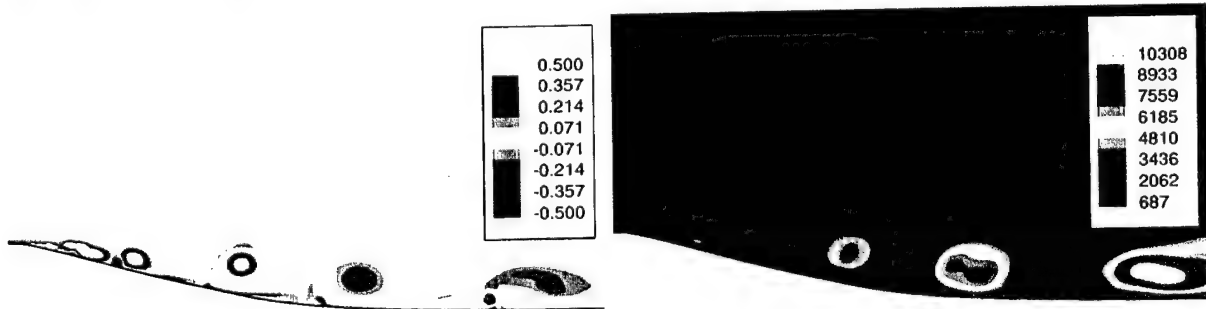
Figure 5.5: 2-D "FSM" computation, $N = 13000$. ω_z isocontours (left) and μ_T/μ isocontours (right).

An instantaneous view of the flow field (see Fig. 5.5) reveals the fairly large-scale turbulent structures. These large "rollers" compare qualitatively to those observed in the "laminar" computations but are, in addition, accompanied by smaller counter-rotating vortices. The eddy viscosity obtained from the turbulence model can easily be associated with the structures visible in the flow as can be observed in Fig. 5.5.

The contribution function f is also closely related to the turbulent structures (see Fig. 5.6). Its
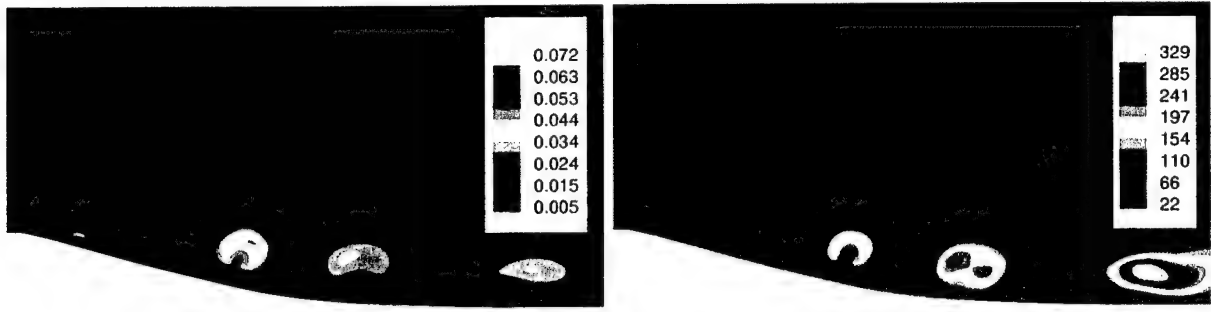
Figure 5.6: 2-D "FSM" computation, $N = 13000$. f isocontours
(left) and $f \mu_T / \mu$ isocontours (right).

maximum values occur in the center of the spanwise "rollers". Since the contribution function is nowhere larger than $\approx 7\%$, the effective eddy viscosity (the part that is fed back into the N-S equations) is considerably smaller than the value provided by the turbulence model.
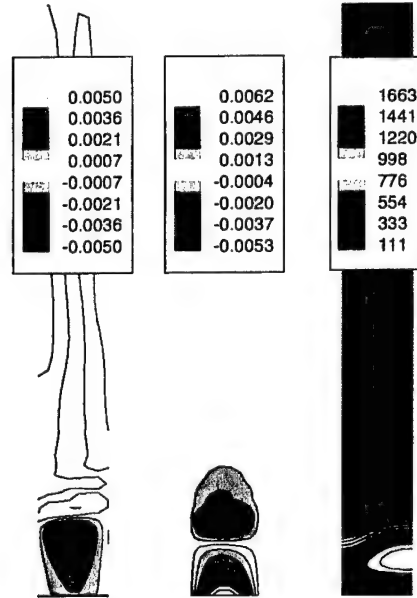
5.4 3-D steady RANS
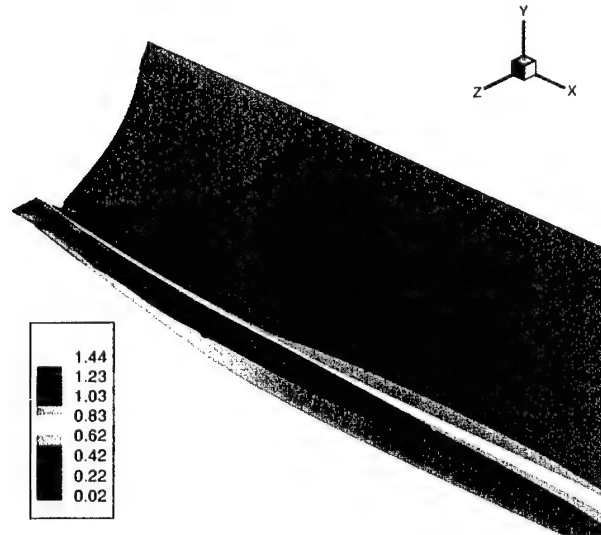
Figure 5.7: 3-D steady RANS. $\omega_x = 0.002$ isosurfaces and u iso-
contours.

The effect of forced longitudinal vortices on the separation bubble was investigated by means of a steady 3-D RANS computation. Steady blowing and suction (with a specified spanwise distribution) of the wall-normal (v) and spanwise (w) velocity components at a disturbance slot upstream

30
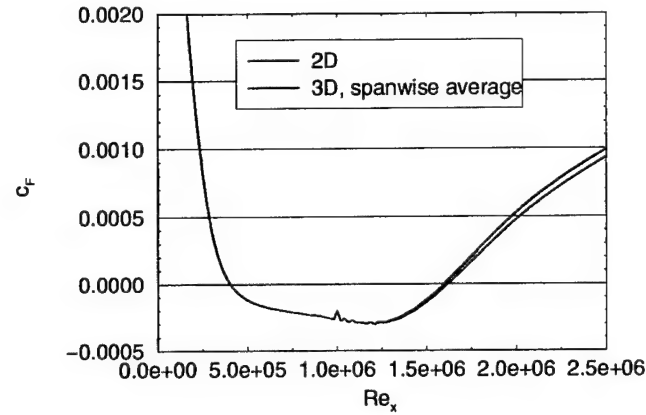
Figure 5.8: 3-D steady RANS. Skin friction coefficient. 2-D computation and 3-D computation with longitudinal vortex (spanwise average).

Figure 5.9: 3-D steady RANS. Slices at constant $x = 150$. Iso-contours of ω_x (left), w, and μ_T/μ (right).

of the ramp is used to introduce a steady longitudinal vortex (see Fig. 5.7). This vortex is first damped and then amplified in streamwise direction in the concave section. Since the effective curvature is small, the amplification is very weak. The influence of the longitudinal vortex on the separation bubble can be observed in the reattachment zone (see Fig. 5.8). The size of the separation bubble is slightly reduced. This computation shows that even a very weak longitudinal

31

vortex can have a considerable impact on the separation behavior. Cross-sectional views reveal the presence of the longitudinal vortex downstream of the reattachment zone (see Fig. 5.9).

6 Stratford Ramp Geometry 2
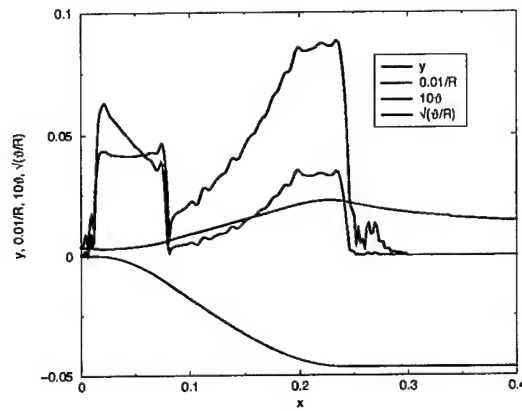
Figure 6.1: Defining parameters for ramp 2 (momentum thickness taken from RANS calculation).

In contrast to the experiments, ramp 1 caused flow separation in our steady RANS computations. As discussed before, because the flow does not stay attached in the concave section, the effective curvature for the separated flow is smaller than for the attached flow. Thus, amplification rates for Görtler vortices are decreased.

The following investigations are therefore carried out using a generic ramp (ramp 2) with stronger concave curvature and a smoother transition from the convex to the concave section (see Fig. 6.1). This ramp does not cause flow separation in our steady RANS computations. The upper wall boundary condition was changed from slip wall to freestream.

The same procedures used to investigate ramp 1 was also applied to ramp 2. First, 2-D "laminar" (with a specified ratio of turbulent to molecular viscosity) and 2-D "FSM" computations were carried out for the purpose of studying the development of unsteady spanwise "rollers". Then,

steady longitudinal vortices were investigated in 3-D RANS computations. Finally, by using full 3-D FSM, an attempt was made to understand the interaction of unsteady 2-D spanwise vortices and steady 3-D longitudinal vortices.

6.1   2-D "laminar" computations

The turbulent eddy viscosity is again assumed to be $\mu_T/\mu = 100$ everywhere. This simple model may not yield the exact flow behavior but allows for computationally inexpensive studies of the dynamics of 2-D large structures.
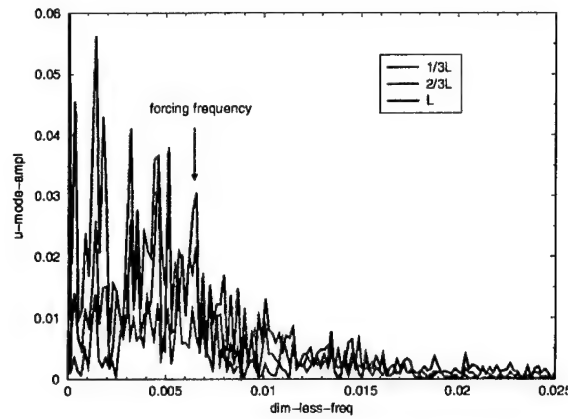
6.1.1   Unforced case
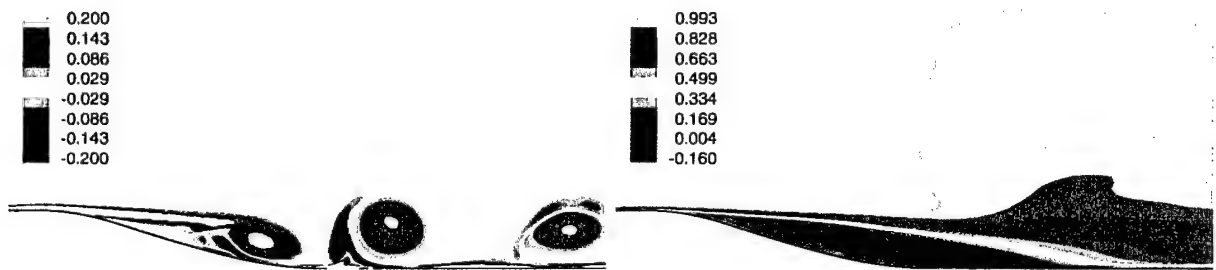
Figure 6.2: 2-D "laminar" computation. ω_z isocontours (instantaneous) (left) and u isocontours (time averaged) (right).

First, an unforced calculation was performed. Fig. 6.3 shows the spectrum from this a calculation for three different downstream locations. The spanwise vortices are very large, hinting at a considerably thickened boundary layer (in the mean) and a large separation bubble (see Fig. 6.2).

6.1.2   Forced case

For the purpose of reattaching the flow, a higher momentum exchange between the more energetic freestream and the retarded boundary layer is desirable. When a frequency peak of the natural case is forced, the control effort can be minimized due to the natural amplification mechanism.

Figure 6.3: 2-D "laminar" computation. Frequency spectrum of u velocity oscillations of unforced calculation at different downstream locations (L is the ramp length).
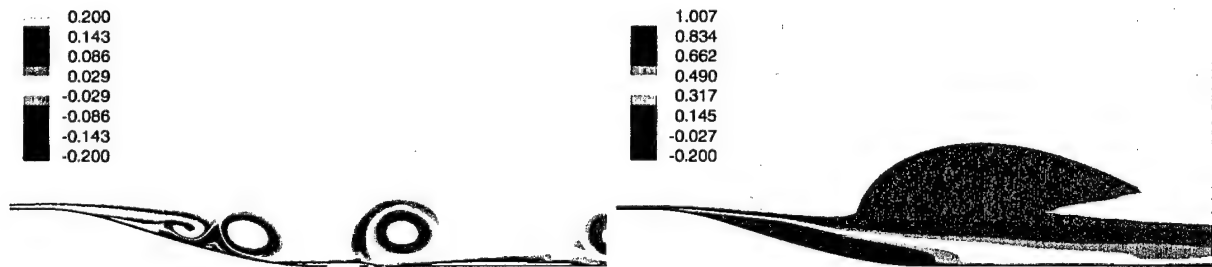
Figure 6.4: 2-D "laminar" computation. ω_z isocontours (instantaneous) (left) and u isocontours (time averaged) (right).

The high-frequency peak of the frequency spectrum taken at $2/3$ of the ramp length (this is at the beginning of the concave section) seems to work best at reducing the spatial extent of the separation bubble. The result of periodic blowing and suction with this frequency upstream of the convex part is shown in Fig. 6.4.

6.2   2-D steady RANS

In a 2-D RANS simulation, the maximum eddy viscosity μ_T/μ is found to be ≈ 400 (see Fig. 6.5). By design, the flow is attached. Due to the strong adverse pressure gradient, the boundary layer thickness grows rapidly.

35
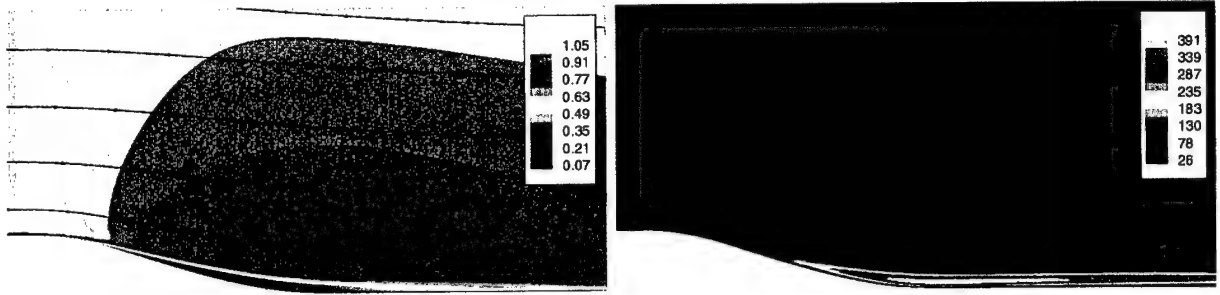
Figure 6.5: 2-D steady RANS. u isocontours (left) and μ_T/μ iso-
contours (right).

6.3   2-D "FSM" computations

If the flow is simulated at the same Reynolds number as in the experiments, the flow is fully turbulent. With the current compressible code setup, a full 3-D DNS of this problem is not yet feasible. The same reasoning as before allows us to investigate the dynamics of 2-D large coherent structures using turbulent 2-D "FSM" simulations. We performed 2-D "FSM" for 3 different values for N (10000, 15000, and 20000) in the contribution function (eq. 4.12).

For $N = 10000$ a large part of the turbulent motion is modeled. The dominating 2-D spanwise vortices are not yet fully resolved (see Fig. 6.6). In the time average, a large separation bubble can be noticed. The contribution function f is nowhere larger than 5%, the maximum of $f\mu_T/\mu$ is about 800.

For $N = 15000$, the contribution of the turbulence model becomes smaller. Unsteady structures become resolved. The large 2-D spanwise vortices are now clearly visible (see Fig. 6.7). They are accompanied by smaller counter-rotating vortices. The maxima of the contribution function can clearly be associated with the structures. The maximum value of the contribution function is about 7%. The effective contribution of the turbulence model $f\mu_T/\mu$ is about 400. The time averaged separation bubble size does not change noticeably compared to the $N = 10000$ case. This is due to the fact that increasing the value of N leads to a better spatial resolution of the large structures but does not change the time averaged flow characteristics.

As N is increased to 20000, the trend continues. Smaller higher-frequency vortices in the ap-
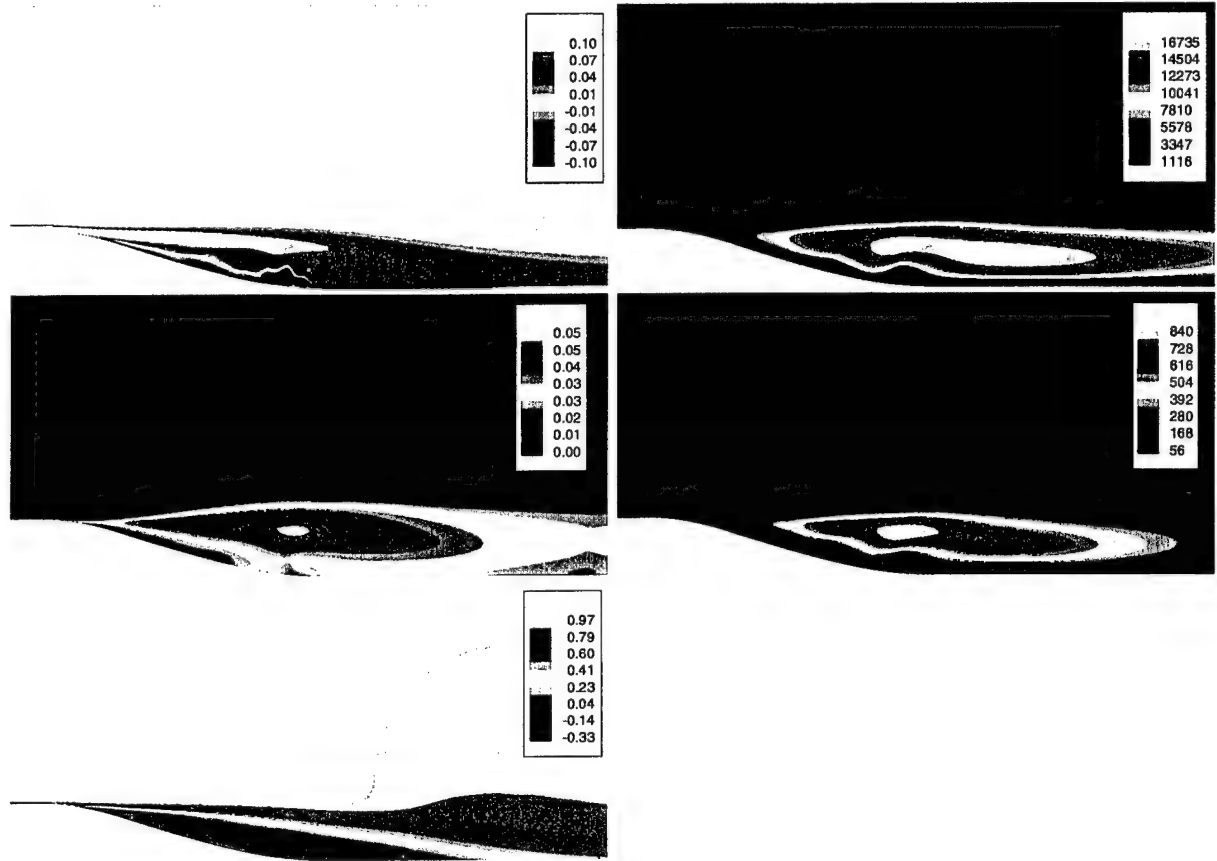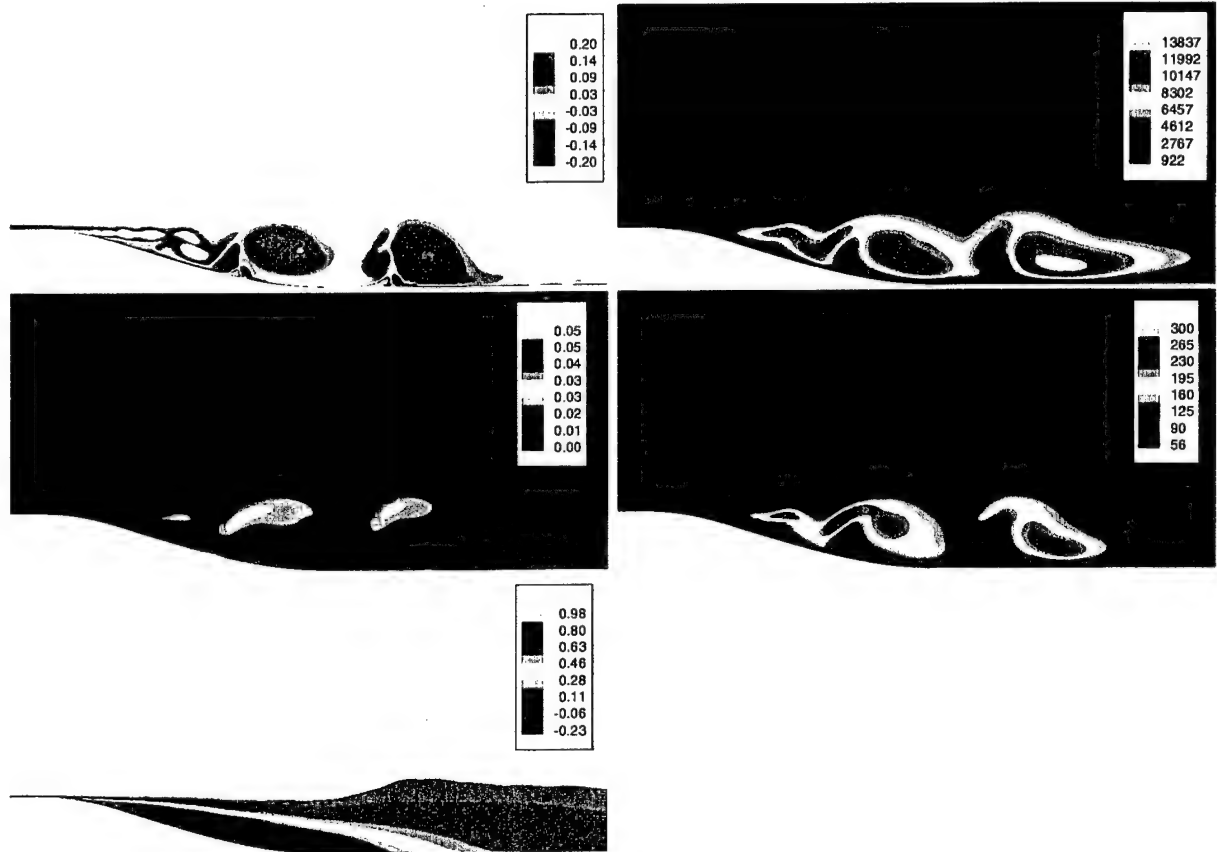
Figure 6.6: 2-D "FSM" computation, $N = 10000$. Top: ω_z iso-
contours (left) and μ_T/μ isocontours (right). Center:
f isocontours (left) and $f\mu_T/\mu$ isocontours (right).
Bottom: u isocontours (time averaged).

proaching boundary layer become resolved (see Fig. 6.8). Vortex merging becomes visible and more small-scale turbulent motion becomes visible in the vicinity of the large-scale structures. The contribution function is about 5%; the effective contribution of the turbulence model $f\mu_T/\mu$ is about 300. Again, the separation bubble size remains essentially unchanged. More and more of the spatial details of the flow appear while the time averaged flow remains unchanged. N cannot be increased much further since the 3-D part of the turbulence motion is neglected in this approach.
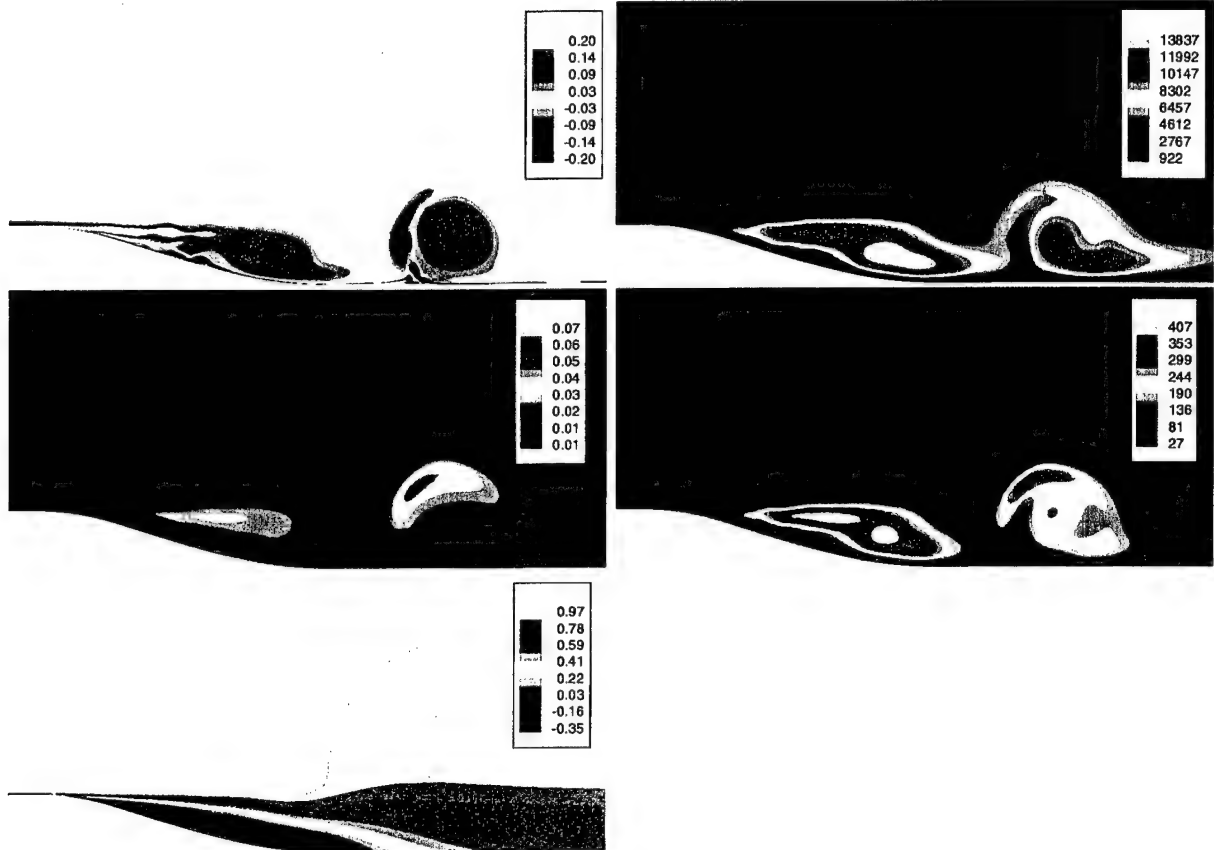
Figure 6.7: 2-D "FSM" computation, $N = 15000$. Top: ω_z iso-contours (left) and μ_T/μ isocontours (right). Center: f isocontours (left) and $f\mu_T/\mu$ isocontours (right). Bottom: u isocontours (time averaged).

Figure 6.8: 2-D "FSM" computation, $N = 20000$. Top: ω_z isocontours (left) and μ_T/μ isocontours (right). Center: f isocontours (left) and $f\mu_T/\mu$ isocontours (right). Bottom: u isocontours (time averaged).

6.4   3-D steady RANS

The characteristics of the steady 3-D longitudinal vortices were studied in 3-D RANS simulations.
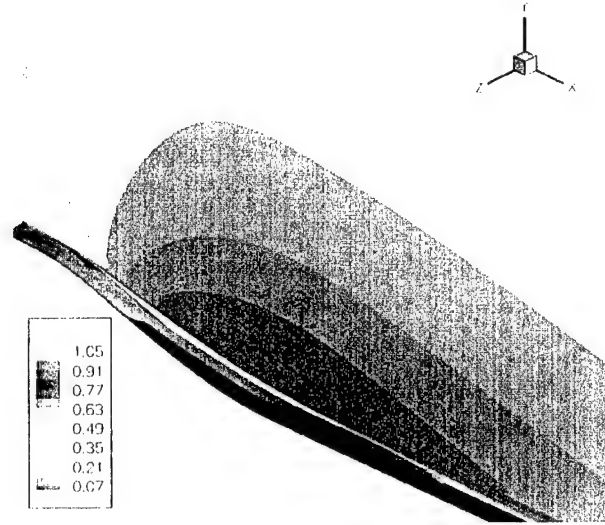
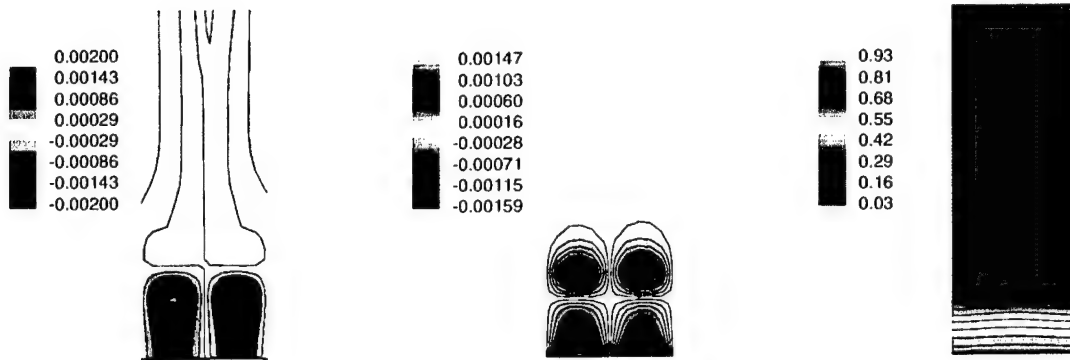**Figure 6.9:** 3-D steady RANS. $L_z = 10$, $\lambda_z = 20$. v and w forcing. $\omega_x = 0.003$ isosurfaces and u isocontours.
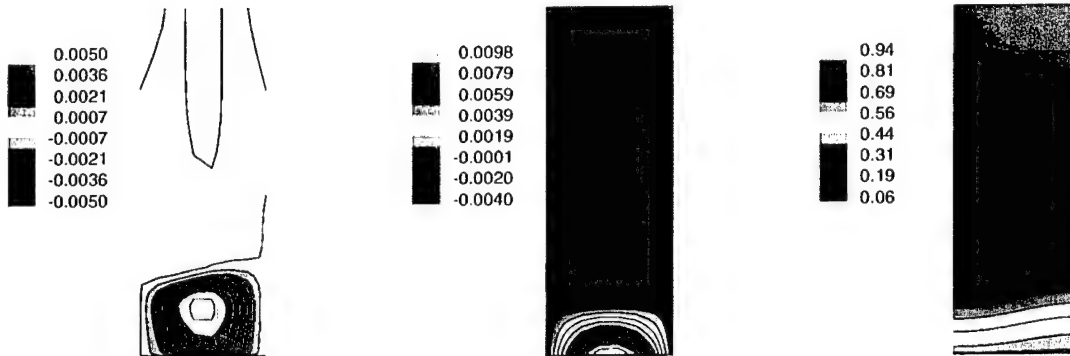
Figure 6.10: 3-D steady RANS. $L_z = 10$, $\lambda_z = 20$. v and w forcing. Slices at constant $x = 150$. Isocontours of ω_x (left), w, and u (right).

First, a spanwise domain width L_z of 10 (non dimensional) was chosen. This corresponds approximately to the largest boundary layer thickness of the 2-D RANS simulation. By prescribing non-zero values for v and w at the wall upstream of the ramp, a steady longitudinal vortex (with spanwise wavelength λ_z of 20) was forced introduced (see Fig. 6.9). This vortex is amplified in the

concave section of the ramp. Cross-sectional views are given in Fig. 6.10. The distribution of the longitudinal vorticity ω_x as well as the distribution of the spanwise velocity w are in accordance with what is expected for Görtler vortices. The boundary layer is distorted by the longitudinal vortex (indicated by the streamwise velocity component u).
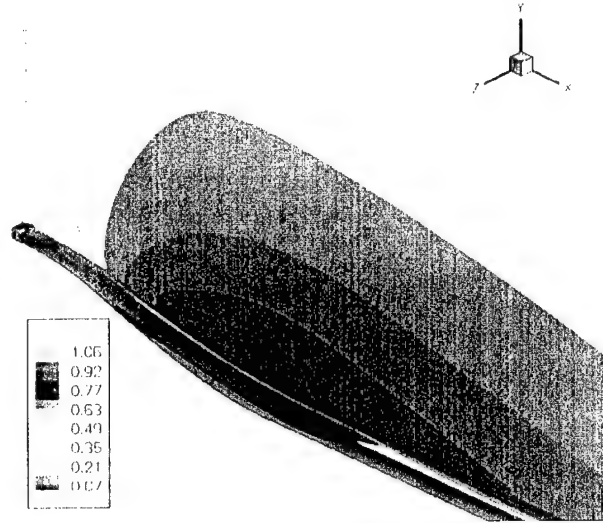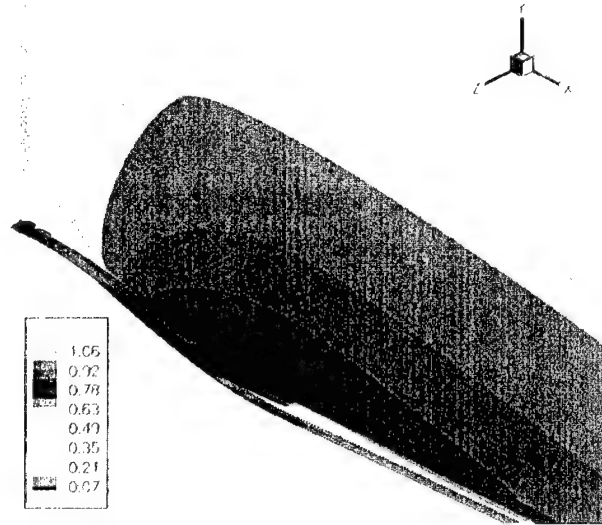

Figure 6.11: 3-D steady RANS. $L_z = 10$, $\lambda_z = 10$. v and w forcing. $\omega_x = -0.001, 0.001$ isosurfaces and u iso-contours.
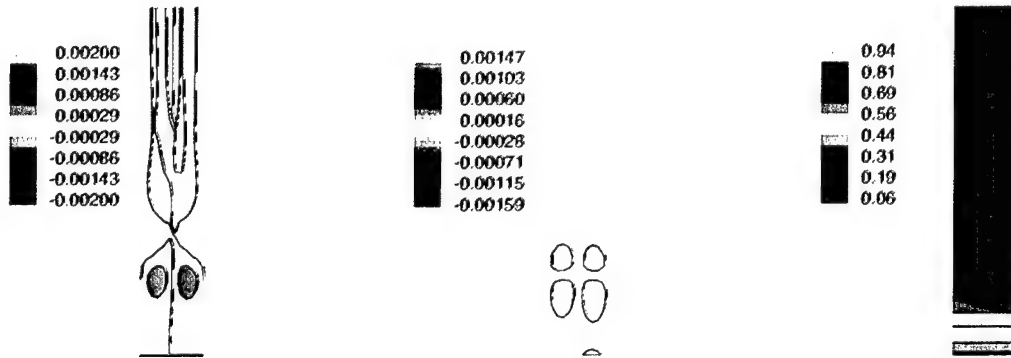

Figure 6.12: 3-D steady RANS. $L_z = 10$, $\lambda_z = 10$. v and w forcing. Slices at constant $x = 150$. Isocontours of ω_x (left), w, and u (right).

Next, two vortices were generated in the same domain (spanwise domain width L_z of 10). Therefore the spanwise wavelength λ_z of the longitudinal structures was halved. The vortices still get

amplified in the concave section but the amplification is smaller (see Fig. 6.11). For cross-sectional views refer to Fig. 6.12. The boundary layer is still slightly distorted by the longitudinal vortices.
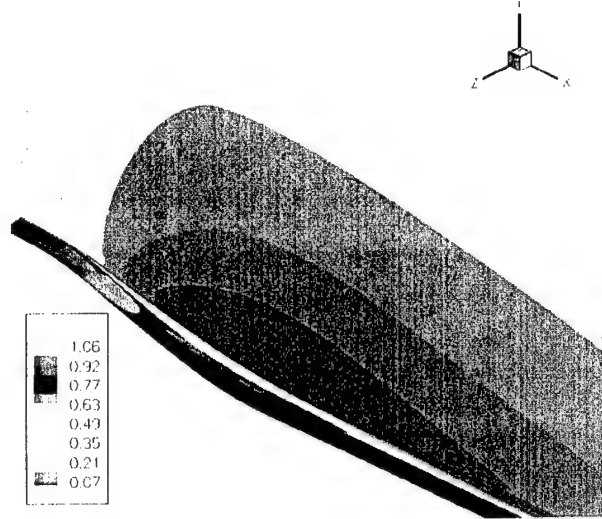

Figure 6.13: 3-D steady RANS. $L_z = 5$, $\lambda_z = 5$. v and w forcing. $\omega_x = -0.001, 0.001$ isosurfaces and u isocontours.
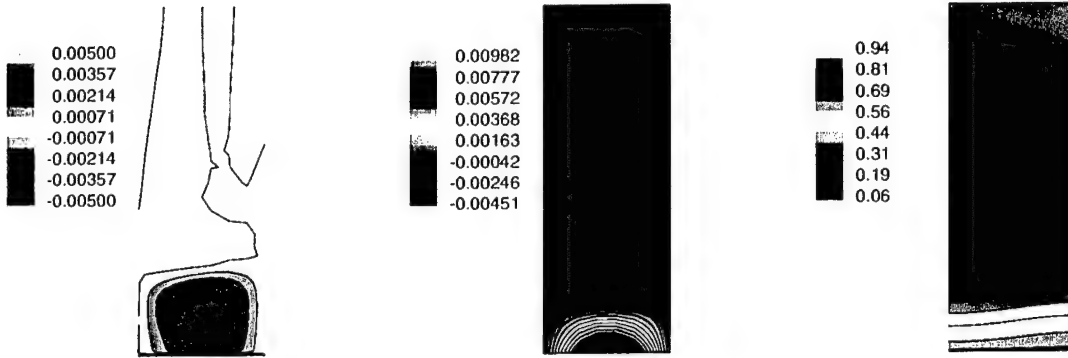

Figure 6.14: 3-D steady RANS. $L_z = 5$, $\lambda_z = 5$. v and w forcing. Slices at constant $x = 150$. Isocontours of ω_x (left), w, and u (right).

Now, the spanwise wavelength was halved once again (by reducing the width of the spanwise domain to L_z to 5). The resulting spanwise wavelength λ_z is 5. The longitudinal vortices are only very slightly amplified (see Fig. 6.13) and are very weak at the $x = 150$ cross-section. The boundary layer appears almost undistorted (see Fig. 6.14). Further reduction of the spanwise wavelength yields a continuation of this trend. Eventually, the vortices will no longer be amplified

and die out shortly downstream of the forcing location.

Figure 6.15: 3-D steady RANS. $L_z = 10$, $\lambda_z = 20$. w forcing. $\omega_x = 0.003$ isosurfaces and u isocontours.
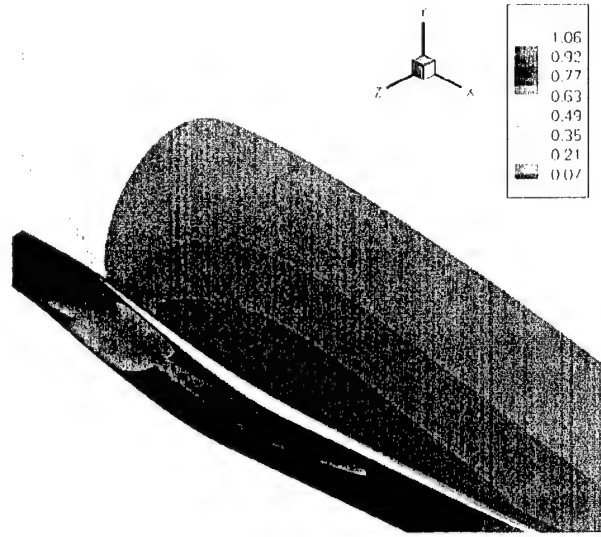

Figure 6.16: 3-D steady RANS. $L_z = 10$, $\lambda_z = 20$. w forcing. Slices at constant $x = 150$. Isocontours of ω_x (left), w, and u (right).

Next, the spanwise domain width L_z is reset to its original width of 10 and only one vortex is forced (the resulting spanwise wavelength λ_z is 20). Only the spanwise (w) component is forced, Thereby reducing the effectiveness of the steady forcing. The resulting longitudinal vortex is weaker (see Fig. 6.15). This becomes apparent by examining the cross-sectional views (see Fig. 6.16) the distortion of the boundary layer.

If the spanwise extent of the computational domain L_z is tripled (this corresponds to a spanwise
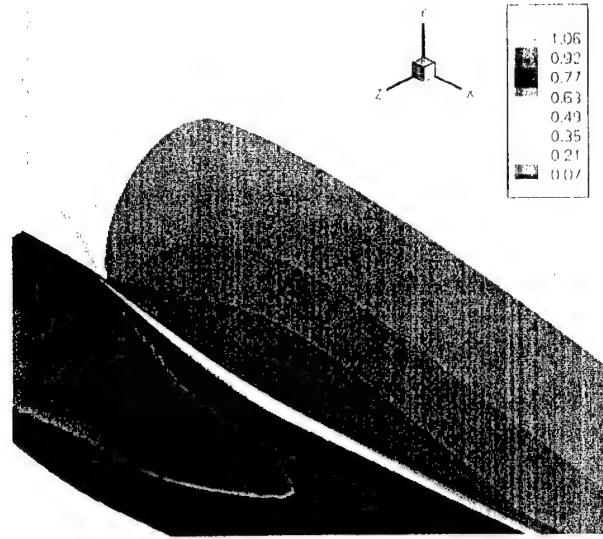
Figure 6.17: 3-D steady RANS. $L_z = 30$, $\lambda_z = 60$. w forcing.
$\omega_x = 0.00035$ isosurfaces and u isocontours.
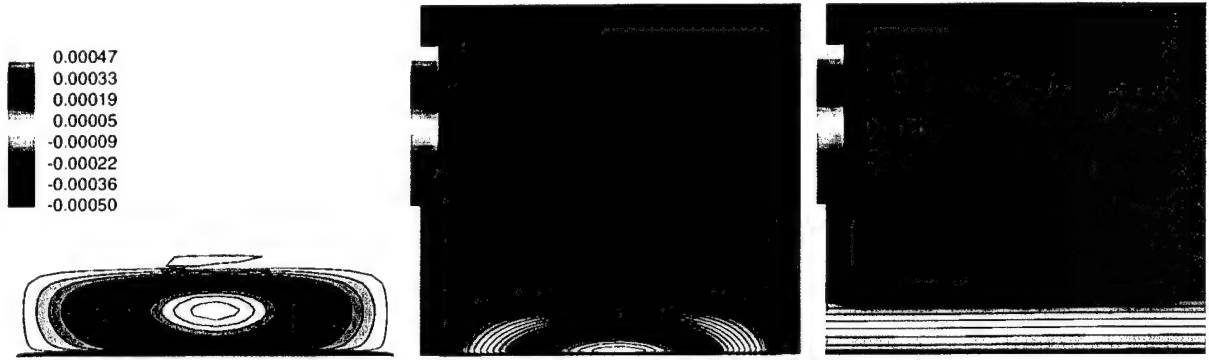
Figure 6.18: 3-D steady RANS. $L_z = 30$, $\lambda_z = 60$. w forcing.
Slices at constant $x = 150$. Isocontours of ω_x (left),
w, and u (right).

wavelength λ_z of 60) the amplification of the longitudinal vortices is greatly reduced (see Fig. 6.17). The cross-sectional views still show the characteristics Görtler vortices (see Fig. 6.18), but the vortex intensity is very low.

If the spanwise domain width L_z is further increased doubled (set to 90; the wavelength of the longitudinal structures λ_z is now 180) the longitudinal vortex is damped (see Fig. 6.19). Cross-sectional views no longer show the Görtler vortex characteristics (see Fig. 6.20). The flow is stable with regard to longitudinal vortices of this wavelength.

Figure 6.19: 3-D steady RANS. $L_z = 90$, $\lambda_z = 180$. w forcing.
$\omega_x = 0.000035$ isosurfaces and u isocontours.
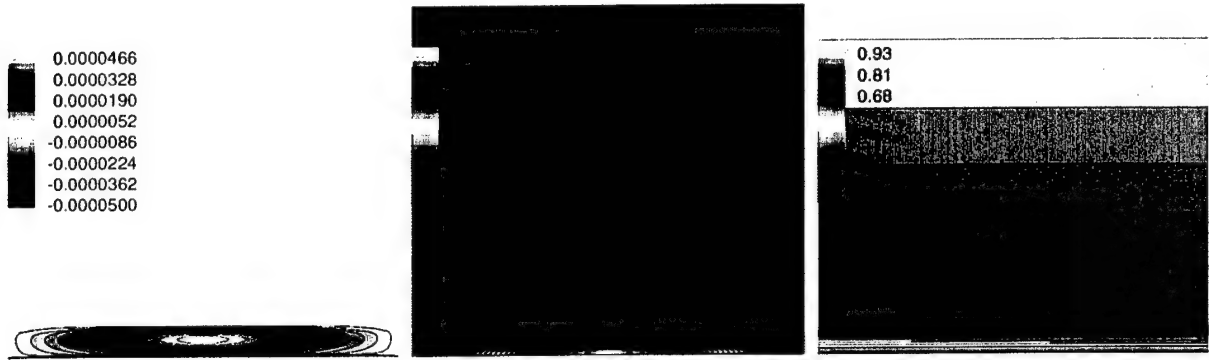
Figure 6.20: 3-D steady RANS. $L_z = 90$, $\lambda_z = 180$. w forcing.
Slices at constant $x = 150$. Isocontours of ω_x (left),
w, and u (right).

This study of various spanwise wavelengths seems to suggest that vortices of wavelength 20 are most amplified. Longitudinal vortex structures can also be generated by a corrugated surface as displayed in Fig. 6.21. The maximum wall displacement in wall normal direction was chosen to be 10% of the domain width. A cylindrical shape was chosen for the geometry deformation in spanwise direction. The wall was formed such that 2 vortices of spanwise wavelength 10 can fit within one valley.

Figure 6.22 shows the 3-D laminar and 3-D RANS test cases as well as the 3-D RANS computa-
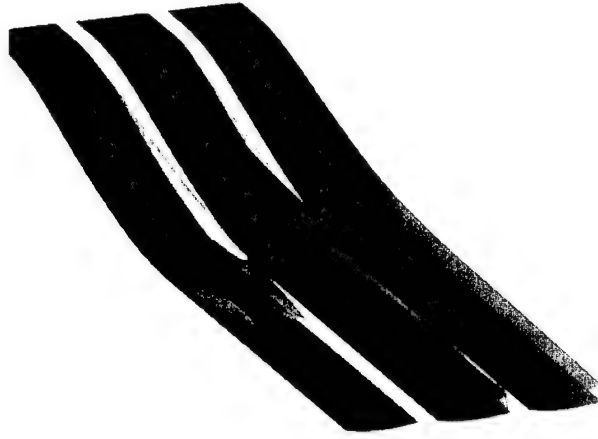
Figure 6.21: 3-D steady RANS. Corrugated surface. Isocontours of $\omega_x = 0.002$ (green), $w = -0.0005, 0.0005$ (red, blue), and $u = 0.737$ (cyan).
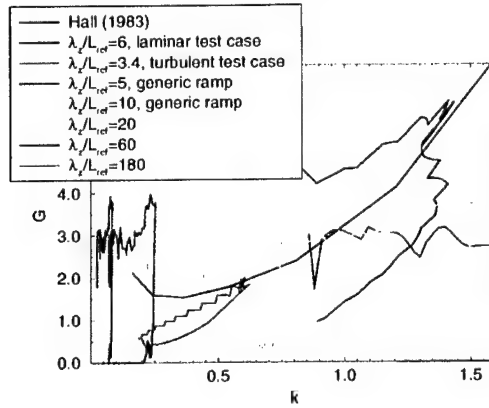
Figure 6.22: Görtler stability diagram.

tions of the generic ramp (ramp 2) in a Görtler stability diagram. The neutral curve of Hall [27] is included for reference. For the turbulence calculations, the viscosity is averaged as

$$\bar{\mu} = \frac{1}{\delta_{99}} \int_0^{\delta_{99}} (\mu + \mu_T) dy , \tag{6.1}$$

where δ_{99} is the local boundary layer thickness. The Görtler number is then computed from the averaged viscosity $\bar{\mu}$. The laminar test case as well as the ramp computations with wavelengths of 10, 20, and 60 are located within the unstable region (which is above Hall's neutral curve). The turbulent test case and the ramp calculations with spanwise wavelengths of 5 and 180 only barely touch the unstable region. Of the various wavelengths chosen in the ramp calculations, wavelength

20 yields the $G(k)$ distribution with most points within the unstable region. This is consistent with the observations made earlier. The longitudinal vortices are most amplified for the case with $\lambda_z/L_{ref} = 20$.

One last remark is in order. The velocity profile in the convex section of the ramp develops a weak outer shear layer, therefore resembling, to some degree, the velocity profile of a wall jet. The Görtler instability mechanism may, as a result, also act in this section of the ramp. It should be noted that a slight amplification of longitudinal vortices in the convex section of the ramp was be observed for most of the cases investigated and discussed in this chapter.

6.5 3-D FSM computations

Finally, 3-D full FSM computations ($N = 20000$, see eq. 4.12) were carried out. The results presented in the following sections are strictly preliminary and are based on simulations that are still in progress. Both forced and unforced cases are being investigated for the purpose of testing our FSM.
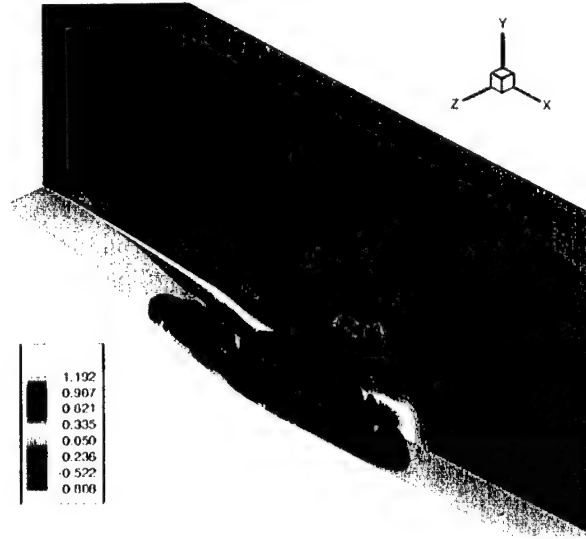
6.5.1 Unforced case
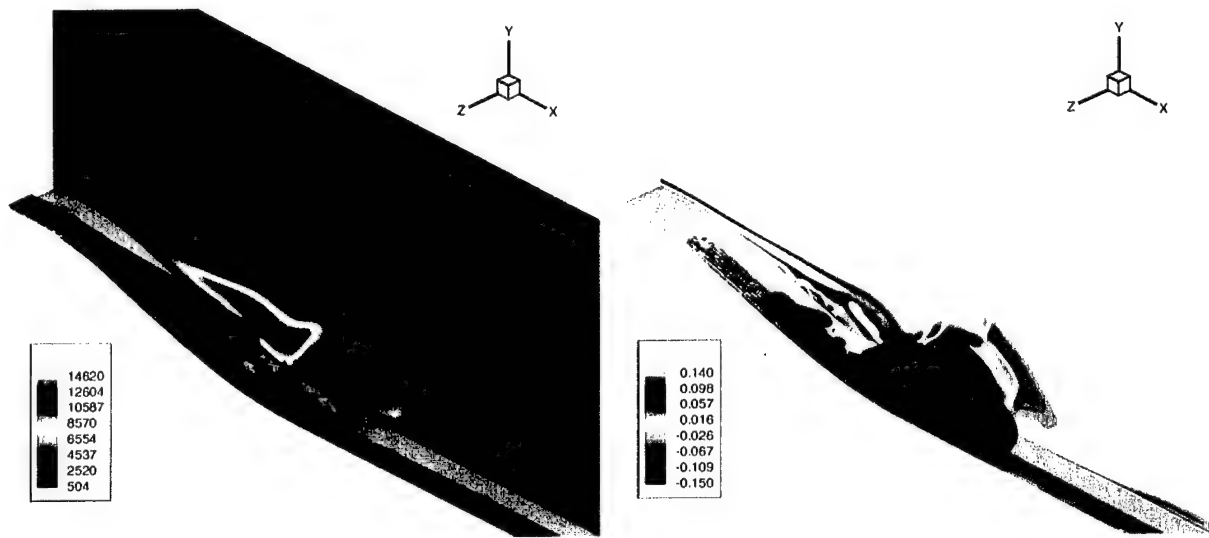
Figure 6.23: 3-D FSM computation. Instantaneous data. Left: Isosurfaces of $\omega_z = -0.1, 0.1$ (red, blue), and iso-contours of μ_T/μ. Right: Isosurfaces of $\omega_x = -0.02, 0.02$ (red, blue), and isocontours of ω_z.

Instantaneous plots of the spanwise vorticity component for the unforced case are shown in Fig. 6.23. Large spanwise structures can be observed. This is consistent with the results obtained from the DNS computations.

Fig. 6.24 shows instantaneous contours of the spanwise velocity component. The apparent three-dimensionality of w clearly indicates the presence of longitudinal structures.

Time-averaged data of the flow field is presented in fig. 6.25. It should be noted that this average was obtained using only a very limited amount of data and can therefore not yet be considered a

Figure 6.24: 3-D FSM computation. Instantaneous data. Isosurfaces of $w = -0.02, 0.02$ (red, blue), and isocontours of u.
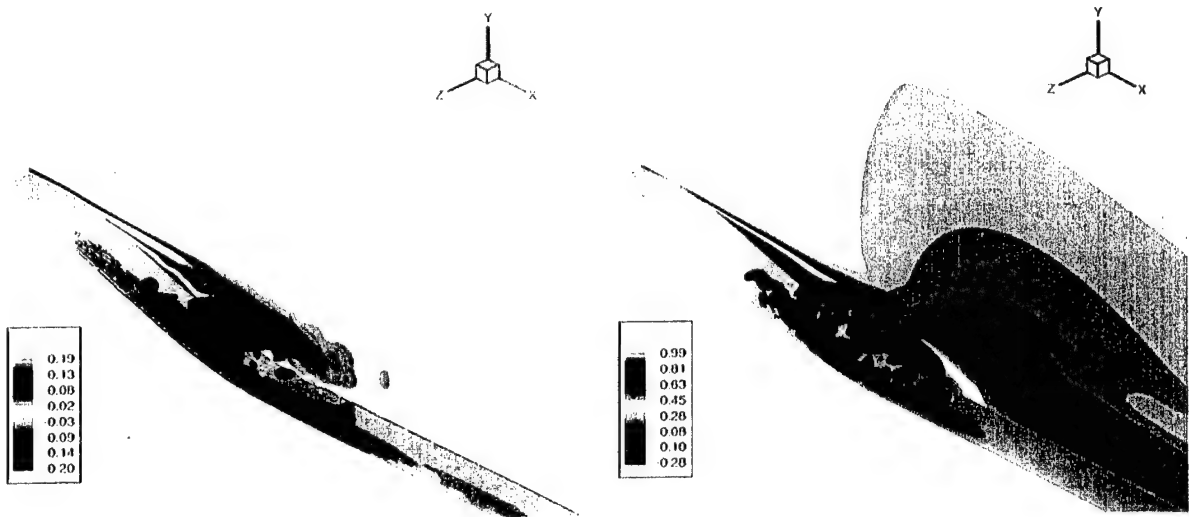
Figure 6.25: 3-D FSM computation. Time averaged data. Left: Isosurfaces of $\omega_x = -0.005, 0.005$ (red, blue), and isocontours of ω_z. Right: Isosurfaces of $w = -0.005, 0.005$ (red, blue), and isocontours of u.

true representation of the flow's mean characteristics. The averaged data does, however, clearly indicate the presence of two distinct longitudinal vortex structures, one close to the wall and the other in the outer region of the boundary layer.

Figure 6.26: 3-D FSM computation. Slices at constant $z = 0$.
Top: ω_z isocontours and μ_T/μ isocontours. Center:
f isocontours and $f\mu_T/\mu$ isocontours. Bottom: u
isocontours (time-averaged).

Slices of constant $z = 0$ are given in fig. 6.26. A clear resemblance to the results from the 2-D "FSM" can be detected. The important difference between the 2-D and 3-D results can be observed in the appearance of small-scale structures in the isocontours of ω_z. The plot of the streamwise velocity component u shows regions of reverse flow. This is believed to be an artifact of the insufficient data available for the averaging. The contribution function shows maxima of about 7%, yielding an effective maximum eddy viscosity of about 400. The contribution of the turbulence model is clearly linked to the presence of the structures.

Instantaneous cross-sectional views at $x = 150$ are shown in Fig. 6.27. The boundary layer is strongly distorted in the spanwise direction, hinting, once again, at the presence of longitudinal vortices. Since this is an unforced calculation, these structures must necessarily appear naturally.
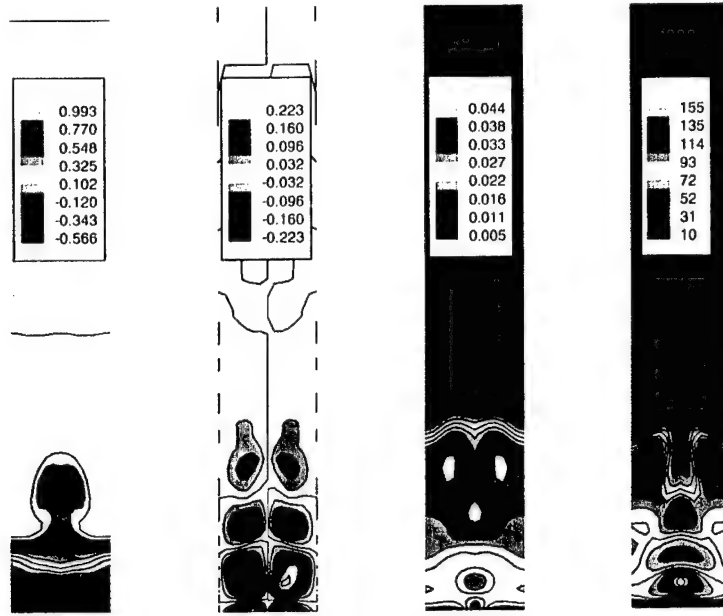
Figure 6.27: 3-D FSM computation. Slices at constant $x = 150$. Isocontours of u, w, f, and $\int \mu_T / \mu$.
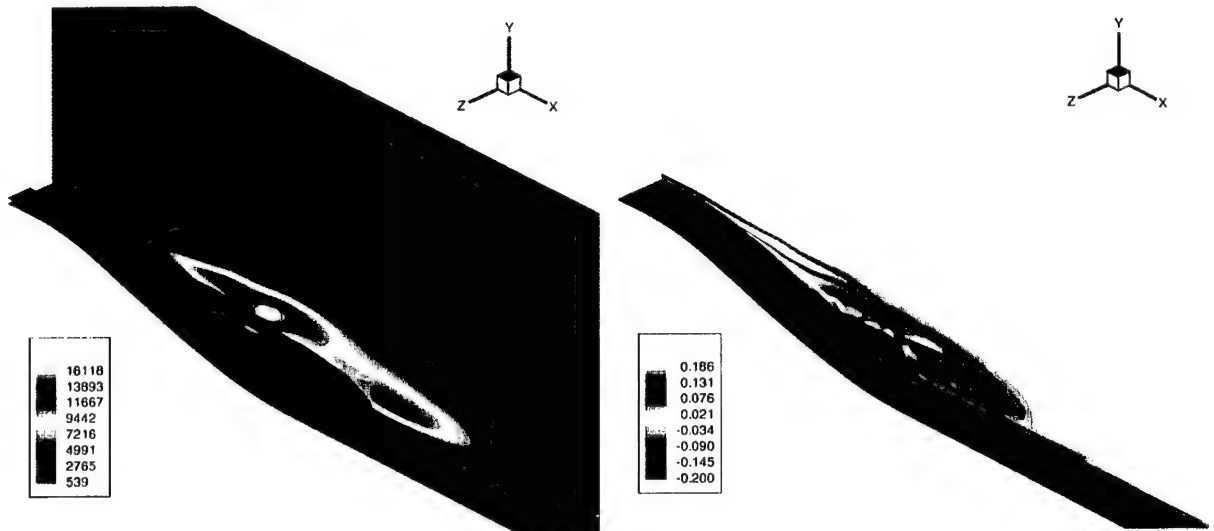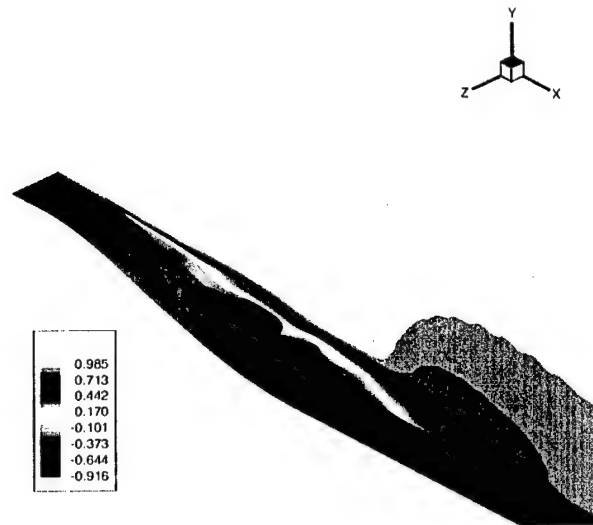
6.5.2 Forced case

Figure 6.28: 3-D FSM computation. Instantaneous data. Left: Isosurfaces of $\omega_z = -0.05, 0.05$ (red, blue), and isocontours of μ_T / μ. Right: Isosurfaces of $\omega_x = -0.02, 0.02$ (red, blue), and isocontours of ω_z.

Figure 6.29: 3-D FSM computation. Instantaneous data. Isosurfaces of $w = -0.02, 0.02$ (red, blue), and isocontours of u.

In addition to the unforced simulation, a second case is being investigated. Longitudinal vortices are introduced upstream of the ramp by steady forcing of the spanwise velocity component w.

Instantaneous pictures of the spanwise and longitudinal vorticity components are presented in fig. 6.28. The spanwise velocity component is shown in fig. 6.29. These results appear similar to those of the unforced case.

Time-averaged results are presented in fig. 6.30, fig. 6.31 and fig. 6.32. The amount of data used for the averaging was once again limited. Nevertheless, the results suggest the fact that the flow can support and sustain longitudinal structures.

At this point, no attempt is made to draw more definite conclusions from the 3-D FSM simulations. The results presented in this section serve the purpose demonstrating to us the functionality and performance of the FSM.
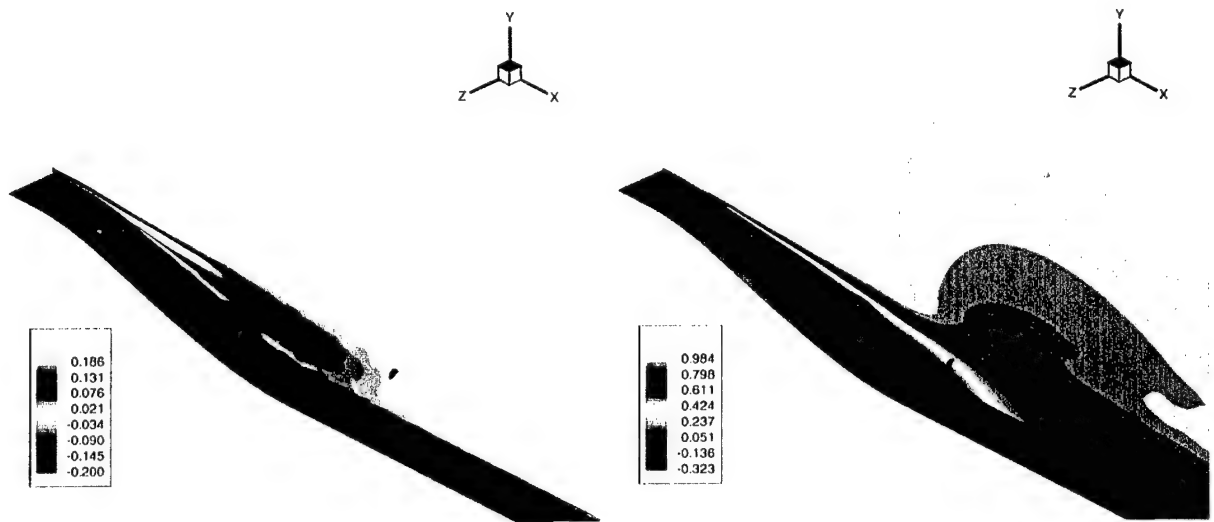
Figure 6.30: 3-D FSM computation. Time averaged data. Left: Isosurfaces of $\omega_x = -0.005, 0.005$ (red, blue), and isocontours of ω_z. Right: Isosurfaces of $w = -0.005, 0.005$ (red, blue), and isocontours of u.

Figure 6.31: 3-D FSM computation. Slices at constant $z = 0$. Top: ω_z isocontours and μ_T/μ isocontours. Center: f isocontours and $f\mu_T/\mu$ isocontours. Bottom: u isocontours (time averaged).
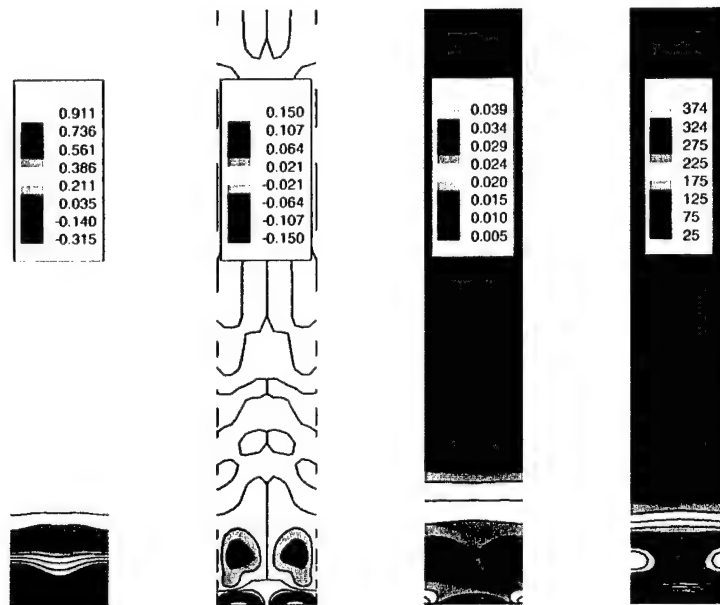
Figure 6.32: 3-D FSM computation. Slices at constant $x = 150$. Isocontours of u (left), w, f, and $f\mu_T/\mu$ (right).

7 Summary

Comprehensive numerical investigations were carried out for the purpose of advancing our understanding of the role of longitudinal vortices in turbulent boundary layers with wall curvature and adverse pressure gradient.

The Stratford ramp geometry, in particular, was studied using DNS, RANS, URANS and FSM. Results obtained from the DNS simulation were scrutinized by means of POD, yielding clear indications for the presence of both two-dimensional structures and three-dimensional longitudinal vortices. In an effort to better understand the complicated dynamics involved, a decision was made to study the underlying phenomena independently. Various numerical tools were developed and applied in order to allow for separate investigations of the two-dimensional and three-dimensional structures, respectively.

A temporal code in cylindrical coordinates was created and utilized for investigations of the Görtler instability mechanism. In addition, a new compressible code in generalized curvilinear coordinates and including an implementation of our FSM was developed. All simulations involving turbulence modeling were carried out using this new code at low Mach number. The FSM was shown to work as expected in fully three-dimensional computations.

The results presented in this report provide strong evidence that dominant coherent structures, both two-dimensional and three-dimensional, are present a Stratford ramp flow. Considerable progress was made in our understanding of the role that these structures play in flows at the verge of separation. Nevertheless, additional research is required before indisputable evidence for their existence and their influence on the flow can be obtained and the physical mechanisms of their

interactions with each other can be understood.

Bibliography

[1] Anderson, J.D. "Hypersonic and High Temperature Gas Dynamics" McGraw-Hill Book Company, 1989

[2] Elsberry, K., Loeffler, J., Zhou, M.D., Wygnanski, I. "An experimental study of a boundary layer that is maintained on the verge of separation" Journal of Fluid Mechanics (2000), vol. 423, pp. 227-261

[3] Elsberry, K., Likhachev, O., Zhou, M.D., Wygnanski, I. "An Experimental and Theroretical Study of a Boundary Layer Approaching Separation" AIAA-96-0867, 1996

[4] Likhachev, O., Neuendorf, R., Wygnanski, I. "On streamwise vortices in a turbulent wall jet that flows over a convex surface" Physics of Fluids, Vol. 13, No. 6, pp. 1822-1825, June 2001

[5] Wilcox, D.C., "'Turbulence Modeling for CFD"' DCW Industries, 1993

[6] Israel, D.M., Fasel, H.F. "Investigation of separation control in compressible boundary layers using periodic disturbances" AIAA-99-3657, 1999

[7] Meitz, H.L. "Numerical Investigation of Suction in a Transitional Flat-Plate Boundary Layer" dissertation, Department of Aerospace and Mechanical Engineering, University of Arizona, 1996

[8] Meitz, H.L., Fasel, H.F. "A compact-difference scheme for the Navier-Stokes equations in vorticity-velocity formulation" Journal of Computational Physics 157, 371-403 (2000)

[9] Stratford, B.S. "The prediction of separation of the turbulent boundary layer" Journal of Fluid Mechanics (1959), vol. 5, pp. 1-16

[10] Stratford, B.S. "An experimental flow with zero skin friction throughout its region of pressure rise" Journal of Fluid Mechanics (1959), vol. 5, pp. 17-35

[11] Visbal, M.R., Gordnier, R.E. "A High-Order Flow Solver for Deforming and Moving Meshes", AIAA-2000-2619, 2000

[12] Zhang, H.L., Fasel, H.F. "Numerical investigation of the evolution and control of two-dimensional unsteady separated flow over a Stratford ramp" AIAA-99-1003, 1999

[13] Zhang, H.L., Fasel, H.F. "Direct numerical simulations of the turbulent flow over a Stratford ramp" AIAA-99-3359, 1999

[14] Zhang, H.L., Bachman, C.R., Fasel, H.F. "Application of a new methodology for simulations of complex turbulent flows" AIAA-2000-2535, 2000

[15] Speziale, C.G. "Turbulence modeling for time-dependent RANS and VLES: a review" AIAA Journal, 36, 2, pp. 173-184, 1998

[16] Zhang, H.L., Fasel, H.F. "Direct Numerical Simulation of Two-Dimensional Incompressible Laminar Flow Over Stratford Ramp" DFD97 Meeting, American Physical Society, November 23-25, San Francisco; *Bull. Amer. Phys. Soc.*, Vol. 42, No. 11, 1997

[17] Fasel, H.F., Bachmann, C., Zhang, H.L. "A New Methodology for Numerical Simulations of Complex Turbulent Flows: From DNS to RANS, A Combined Approach" *Interim Report to ONR*, 1998

[18] Volino, R.J., Simon, T.W. "Measurements in a Transitional Boundary Layer with Goertler Vortices" Trans. *ASME, J. Fluids Eng.*, Vol. 119, pp. 562-568., 1997

[19] So, R.M.C., Mellor, G.L. "Experiment on the Turbulent Boundary Layers on a Concave Wall", *Aero. Q.*, Vol. 26, pp. 25-40, 1975

[20] Jiang, G.-S., Wu, C.-C. "A High-Order WENO Finite Difference Scheme for the Equations of Ideal Magnetohydrodynamics" Journal of Computational Physics **150**, 561-594 (1999)

[21] Balsara, D.S., Shu, C.-W. "Monotonicity Preserving Essentially Non-oscillatory Schemes with Increasingly High Order of Accuracy" Journal of Computational Physics **160**, 405-452 (2000)

[22] Roe, P.L. "Approximate Riemann Solvers, Parameter Vectors and Difference Schemes" Journal of Computational Physics **43**, 357-372 (1981)

[23] Cullen, L.M., Nishri, B., Greenblatt, D., Wygnanski, I. "The Influence of Curvature on Flow over the Stratford Ramp" to appear at 40th AIAA Aerospace Sciences, Reno, NV, Jan. 2002

[24] Rayleigh, Lord "On the dynamics of revolving fluids" Scientific Papers 6: 447-453, Cambridge: Cambridge Univ. Press., 1916

[25] Saric, W.S. "Görtler Vortices" Annu. Rev. Fluid Mech. 1994. 26:379-409

[26] Görtler, H. "Instabilität laminarer Grenzschichten an konkaven Wänden gegenüber gewissen dreidimensionalen Störungen" ZAMM 21 250-52; also NACA Rep. 1375 (1954)

[27] Hall, P. "The linear development of Görtler vortices in growing boundary layers" Journal of Fluid Mechanics (1983), vol. 130, pp. 41-58

[28] Sabry, A.S., Liu, J.T.C. "Longitudinal vorticity elements in boundary layers: nonlinear development from initial Görtler vortices as a prototype problem" Journal of Fluid Mechanics (1991), vol. 231, pp. 615-663

[29] Swearingen, J.D., Blackwelder, R.F. "The growth and breakdown of streamwise vortices in the presence of a wall" Journal of Fluid Mechanics (1987), vol. 128, pp. 255-290

[30] Patel, V.C., Sotiropoulos, F. "Longitudinal Curvature Effects in Turbulent Boundary Layers" Prog. Aerospace Sci. Vol. 33, pp 1-70, 1997

[31] Barlow, R.S., Johnston, J.P. "Structure of a turbulent boundary layer on a concave surface" Journal of Fluid Mechanics (1988), vol. 191, pp. 137-176

[32] Moser, R.D., Moin, P. "The effects of curvature in wall-bounded turbulent flows" Journal of Fluid Mechanics (1987), vol. 175, pp. 479-510

[33] Tani, I. "Production of Longitudinal Vortices in the Boundary Layer along a Concave Wall" J. Geophys. Res. **67**, 3075-3080, 1962

[34] Harris, P.J. "Numerical Investigation of Transitional Compressible Plane Wakes" dissertation, University of Arizona, 1997

[35] Ferziger, J.H. "Numerical Methods for Engineering Application" John Wiley & Sons, 1981